Description and Evaluation of the MIT Earth System Model (MESM)

Journal of Advances in Modeling Earth Systems

RESEARCH ARTICLE
10.1029/2018MS001277

Key Points:
- Climate sensitivity and rate of ocean heat uptake of the MIT Earth System Model can be varied over wide ranges to address uncertainty
- Computational efficiency of the Model allows us to run large ensembles of simulations for robust uncertainty quantification
- The inclusion of an atmospheric chemistry model allows us to perform emission-driven simulations and evaluate impacts of different policies on future climate

Correspondence to:
A. Sokolov,
sokolov@mit.edu

Citation:
Sokolov, A., Kicklighter, D., Schlosser, A., Wang, C., Monier, E., Brown-Steiner, B., et al. (2018). Description and Evaluation of the MIT Earth System Model (MESM). *Journal of Advances in Modeling Earth Systems*, *10*, 1759–1789. https://doi.org/10.1002/2018MS001277

Received 29 JAN 2018
Accepted 2 JUL 2018
Accepted article online 10 JUL 2018
Published online 3 AUG 2018
Corrected 15 AUG 2018

This article was corrected on 15 AUG 2018. See the end of the full text for details.

Description and Evaluation of the MIT Earth System Model (MESM)

Andrei Sokolov[1], David Kicklighter[2], Adam Schlosser[1], Chien Wang[1], Erwan Monier[1], Benjamin Brown-Steiner[1,3], Ronald Prinn[1], Chris Forest[4], Xiang Gao[1], Alex Libardoni[4], and Sebastian Eastham[5]

[1]Joint Program on the Science and Policy of Global Change, Massachusetts Institute of Technology, Cambridge, MA, USA, [2]The Ecosystems Center, Marine Biological Laboratory, Woods Hole, MA, USA, [3]Now at Atmospheric and Environmental Research, Lexington, MA, USA, [4]Department of Meteorology and Earth and Environmental Systems Institute, Pennsylvania State University, University Park, PA, USA, [5]Laboratory for Aviation and the Environment, Department of Aeronautics and Astronautics, Massachusetts Institute of Technology, Cambridge, MA, USA

Abstract The Massachusetts Institute of Technology Integrated Global System Model (IGSM) is designed for analyzing the global environmental changes that may result from anthropogenic causes, quantifying the uncertainties associated with the projected changes, and assessing the costs and environmental effectiveness of proposed policies to mitigate climate risk. The IGSM consists of the Massachusetts Institute of Technology Earth System Model (MESM) of intermediate complexity and the Economic Projections and Policy Analysis model. This paper documents the current version of the MESM, which includes a two-dimensional (zonally averaged) atmospheric model with interactive chemistry coupled to the zonally averaged version of Global Land System model and an anomaly-diffusing ocean model.

1. Introduction

There is significant uncertainty in projections of future climate associated with uncertainty in possible pathways of economic development and corresponding anthropogenic emissions of different gases as well as with uncertainty in climate system response to these emissions. Climate system properties that determine its response to transient forcing differ significantly among simulations of atmosphere-ocean general circulation models (AOGCMs, e.g., Andrews et al., 2012; Forster et al., 2013; Intergovernmental Panel on Climate Change, IPCC, 2013) and Earth System Models (ESMs, Friedlingstein et al., 2006, 2014) leading to a large spread in projected future atmospheric CO_2 concentrations and radiative forcing for a given emission scenario. These properties include climate sensitivity, the rate at which the deep ocean absorbs heat, and the strength of the carbon cycle and carbon-climate feedbacks. There are additional uncertainties in the forcing itself, especially in the forcing associated with aerosol-cloud interaction.

Unfortunately, the available directly measured ocean, land, and atmospheric data can only place limited constraints on some of these key quantities (e.g., Andronova & Schlesinger, 2001; Forest et al., 2008; Gregory et al., 2002; Libardoni & Forest, 2011). As a result, uncertainties in climate sensitivity or aerosol forcing have not been reduced over the last few decades in spite of significant efforts and are unlikely to be substantially reduced within the next decade or more, when important policy choices must nevertheless be made. These uncertainties, in turn, result in a rather wide uncertainty in projected future climate change.

To place our current understanding of potential future climate change within the context of these uncertainties, the latest report of Intergovernmental Panel on Climate Change (IPCC, 2013) provides probability intervals for projected changes of future climate, based on a multimodel ensemble (MME). There are, however, well-known problems with MMEs, such as small sample size and the fact that different models are neither independent nor equally plausible (IPCC, 2013, and literature referenced there). In addition, there are no guaranties that the existing AOGCMs and ESMs sample the full ranges of uncertainties in different climate characteristics, consistent with observed climate change, or moreover, sample these ranges systematically. An alternative approach is to estimate the probability distributions of climate parameters based on available data for past climate and then carry out large (few hundred members) ensembles of future climate simulations by sampling parameter values from these distributions. Even with much greater computational power than is available today, however, it will not be possible to carry out

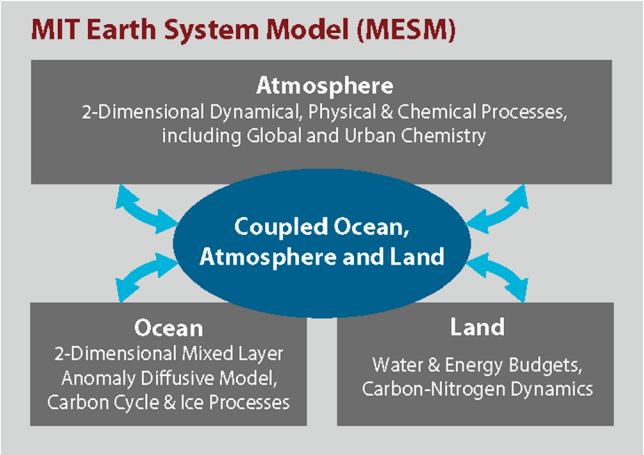

Figure 1. Massachusetts Institute of Technology Earth System Model of intermediate complexity (MESM).

such an exercise using a fully complex state-of-the-art AOGCM or ESM. Therefore, such studies (Knutti et al., 2003; Rogelj et al., 2012; Sokolov et al., 2009; Webster et al., 2003, 2012) are usually carried out with Earth System Models of Intermediate Complexity (EMICs).

The EMICs occupy a place between simple conceptual models and comprehensive global circulation models (Claussen et al., 2002). It has been shown that, with an appropriate choice of parameter values, EMICs can reproduce global mean changes simulated by different AOGCMs and ESMs under different forcing scenarios (Meinshausen et al., 2011; Raper et al., 2001; Sokolov et al., 2003). Model intercomparisons also have shown that in many cases changes in climate predicted by models of intermediate complexity are very similar to those obtained in the simulations with AOGCMs (Gregory et al., 2005; Stouffer et al., 2006).

The structure and complexity of different submodels of a particular EMIC depend on the type of issues to be addressed by the model. The Massachusetts Institute of Technology (MIT) Earth System Model (MESM) is designed to provide the flexibility and computational speed required to handle uncertainty analyses while also representing more detailed physics, chemistry, and biology closer to that of the more computationally intensive ESMs. Within the MIT Integrated System Model (IGSM), the MESM is linked to a model of human interactions, the Economic Projections and Policy Analysis (EPPA) model (Y.-H. Chen et al., 2016), so that the consequences of various economic and policy decisions on future climate may be evaluated. In previous publications, the acronym *IGSM* was used for both the Integrated System Model as a whole (i.e., MESM plus EPPA) and its climate component (i.e., MESM alone). Here we use the acronym *MESM* for the latter.

The MESM can be run in both concentration-driven and emissions-driven modes. As a result, it can be used to quantify uncertainties in future climate. To do this, the MESM is first used to produce probability distributions for the climate sensitivity, the rate of heat uptake by the deep oceans, and the net forcing due to aerosol-radiation interaction by comparing observed temperature changes over the twentieth century with the results of historical (concentration-driven) simulations in which model parameter values are varied over wide ranges (Forest et al., 2002, 2008; Libardoni, 2017; Libardoni & Forest, 2011, 2013). The constructed distributions are then used to carry out ensembles of future climate emissions-driven simulations and produce probability distributions for changes in different climate variables. Uncertainty in climate system response is then combined with uncertainty in anthropogenic emissions (Webster et al., 2002, 2008) to estimate overall uncertainty in possible anthropogenic climate change (Sokolov et al., 2009; Webster et al., 2003, 2012). The first version of the MESM, developed in the mid-1990s (Prinn et al., 1999; Sokolov & Stone, 1995, 1998), has since been continually modified and extended (Sokolov et al., 2005). Different versions of the MESM have been used in a number of model intercomparison projects (e.g., Brasseur et al., 2016; Brovkin et al., 2006; Eby et al., 2013; Gregory et al., 2005; Petoukhov et al., 2005; Plattner et al., 2008; Olsen et al., 2013; Stouffer et al., 2006; Zickfeld et al., 2013). The MESM shows generally comparable results to those of more complex models. For example, a study of the impact of aviation emissions on atmospheric chemical composition and climate shows that the MESM performs within the envelope of the more complex 3-D chemistry-climate models (Brasseur et al., 2016; Olsen et al., 2013).

In this paper, we describe the current version of the MESM, as of the middle of 2017. Description of the model components is given in section 2. Section 3 provides a comparison of simulated present-day climate and historical climate change with results produced by CMIP5 models and available observations.

2. Model Description

The major model components of the MESM (Figure 1) include the following:

1. an atmospheric dynamics, physics, and chemistry model, which includes a submodel of urban chemistry;
2. an ocean model with carbon cycle and sea ice submodels; and
3. a linked set of coupled process-based land models: the Terrestrial Ecosystem Model (TEM), a fully integrated Natural Emissions Model (NEM), and the Community Land Model (CLM), that simulate

terrestrial water, energy, carbon, and nitrogen budgets including carbon dioxide (CO_2) and trace gas emissions of methane (CH_4) and nitrous oxide (N_2O).

The earth system depicted in Figure 1 represents a fully coupled system that allows simulation of critical feedbacks among its components. Time steps used in the various submodels range from 10 min for atmospheric dynamics, to 1 month for TEM, reflecting differences in the characteristic time scales of different processes simulated by the MESM. The major model components of the MESM and linkages are summarized below.

2.1. Atmospheric Dynamics and Physics

The MIT two-dimensional (2-D) atmospheric dynamics and physics model (Sokolov & Stone, 1998) is a zonally averaged statistical dynamical model that explicitly solves the primitive equations for the zonal mean state of the atmosphere and includes parameterizations of heat, moisture, and momentum transports by large-scale eddies based on baroclinic wave theory (Stone & Yao, 1987, 1990). The model's numerics and parameterizations of physical processes, including clouds, convection, precipitation, radiation, boundary layer processes, and surface fluxes, build upon those of the Goddard Institute for Space Studies (GISS) GCM (Hansen et al., 1983). The radiation code includes all significant greenhouse gases (H_2O, CO_2, CH_4, N_2O, CFCs, and O_3) and multiple types of aerosols (e.g., SO_2, black and organic carbon). Anthropogenic aerosol is treated differently in concentration-driven and emissions-driven simulations. In historical simulations, forcing due to anthropogenic aerosol is parameterized through changes in surface albedo using historical data on SO_2 emissions. In future climate simulations, concentrations of SO_2, black and organic carbon are calculated by the chemistry model using emissions provided by the EPPA model. The model does not have any parameterization of indirect aerosol effects; however, the strength of the aerosol forcing can be varied.

The model's horizontal and vertical resolutions are variable, but the standard version of the MESM has 4° resolution in latitude and 11 levels in the vertical.

The MIT 2-D atmospheric dynamics and physics model allows up to four different types of surfaces in the same grid cell (ice-free ocean, sea ice, land, and land ice). The surface characteristics (e.g., temperature, soil moisture, and albedo) as well as turbulent and radiative fluxes are calculated separately for each kind of surface, while the atmosphere above is assumed to be well-mixed horizontally in each latitudinal band. The area weighted fluxes from different surface types are used to calculate the change of temperature, humidity, and wind speed in the atmosphere. The moist convection parameterization, which was originally designed for the GISS Model I (Hansen et al., 1983), requires knowledge of subgrid-scale temperature variance. Zonal temperature variance associated with transient eddies is calculated using a parameterization proposed by Branscome (see Stone & Yao, 1987). The variance associated with stationary eddies is represented by adding a fixed variance that follows more closely the climatological pattern (see Figure. 7.8b of Peixoto & Oort, 1992). In addition, the threshold values of relative humidity for the formation of large-scale cloud and precipitation vary with latitude to account for the dependence of the zonal variability of relative humidity on latitude. Zonal precipitations simulated by the atmospheric model are partitioned into land and ocean components using present-day climatology. These changes led to an improvement in the zonal pattern of the annual cycle of land precipitation and evapotranspiration (Schlosser et al., 2007). While the land/ocean partition of precipitation will likely be changing over time, it is kept fixed in our simulations.

The atmospheric model's climate sensitivity can be changed by varying the cloud feedback. Namely, the cloud fraction used in radiation calculation (C^{rad}) is adjusted as follows:

$$C^{rad} = C^{\circ} \cdot (1.0 + \kappa \cdot \Delta T_{srf}), \quad (1)$$

where C^{o} is a cloud fraction simulated by the model, ΔT_{srf} is the difference of the global-mean surface air temperature from its values in the control climate simulation, and κ is a parameter used to vary climate sensitivity. The unperturbed climate sensitivity of the current version of MESM is 2.8 K. Climate sensitivity for the given value of κ is calculated from an equilibrium $2 \times CO_2$ simulations with mixed layer ocean model.

This method was proposed by Hansen et al. (1993) and was extensively tested in simulations with the MIT climate model (Sokolov & Stone, 1998). The choice of cloud feedback seems very natural because

differences in climate sensitivity between different AOGCMs are to a large extent caused by large differences in this feedback (Bony et al., 2006; Cess et al., 1990; Colman, 2003; Webb et al., 2006; Williams et al., 2006). The method was later modified by using κ of different signs for high and low clouds (Sokolov, 2006), accounting for the fact that the feedback associated with changes in cloud cover has different signs for high and low clouds. Therefore, using different signs in equation (1) depending on cloud heights minimizes the value of κ required to obtain a specific value of climate sensitivity. In addition, the use of the modified method improves the agreement in simulated changes in surface fluxes between the MIT climate model and different AOGCMs. This approach to changing climate sensitivity was also tested in simulations with CAM3 (Sokolov & Monier, 2012), by comparison with a perturbed physics approach. This approach, while allowing climate sensitivity to systematically change over a wide range, does not reproduce uncertainty in geographical structure of surface warming.

2.2. Urban and Global Atmospheric Chemistry

To calculate atmospheric composition, the model of atmospheric chemistry includes the chemistry of climate-relevant gases and aerosols at two domains: the urban scale and the global scale. The urban model is a subgrid-scale chemistry model whose emissions and pollutants are exported (along with emissions from nonurban areas) into the 2-D global zonal-mean model of atmospheric chemistry, which is linked to the atmospheric dynamics and physics model described above. This atmospheric model provides wind speeds, temperatures, solar radiation fluxes, and precipitation to both the urban and global-scale chemistry models. The details of the subgrid-scale urban chemistry model and the 2-D zonal-mean atmospheric chemistry model, and their coupling, are described below.

2.2.1. Urban Atmospheric Chemistry

Urban emissions and air pollution have a significant impact on global methane, ozone, and aerosol chemistry, and thus on the global climate. However, the nonlinearities in the chemistry cause urban emissions to undergo different net transformations than rural emissions, and thus urban chemistry is treated separately from nonurban emissions within the MESM. Accuracy in describing these transformations is necessary because the atmospheric life cycles of exported air pollutants such as CO, O_3, NO_x, and VOCs, and the climatically important species CH_4 and sulfate aerosols, are linked through the fast photochemistry of the hydroxyl free radical (OH) as we will emphasize in the results discussed later in section 3. Urban air shed conditions need to be resolved at varying levels of pollution. The urban air chemistry model must also provide detailed information about particulates and their precursors important to air chemistry and human health, and about the effects of local topography and structure of urban development on the level of containment and thus the intensity of air pollution events. This is an important consideration because air pollutant levels are dependent on projected emissions per unit area, not just total urban emissions.

The urban atmospheric chemistry model has been introduced as an additional component to the original global model (Prinn et al., 1999) in MESM (Calbó et al., 1998; Mayer et al., 2000; Prinn et al., 2007). It was derived by fitting multiple runs of the detailed 3-D California Institute of Technology (CIT) Urban Airshed Model, adopting the probabilistic collocation method to express outputs from the CIT model in terms of model inputs using polynomial chaos expansions (Tatang et al., 1997). This procedure results in a reduced format model to represent about 200 gaseous and aqueous pollutants and associated reactions over urban areas that is computationally efficient enough to be embedded in the global model. The urban module is formulated to take meteorological parameters including wind speed, temperature, cloud cover, and precipitation as well as urban emissions as inputs. Calculated with a daily time step, it exports fluxes along with concentrations (peak and mean) of selected pollutants to the global model.

2.2.2. Global Atmospheric Chemistry

The 2-D zonal-mean model that is used to calculate atmospheric composition is a finite difference model in latitude-pressure coordinates, and the continuity equations for the trace constituents are solved in mass conservative, of flux, form (see Wang et al., 1998 for a more complete description). The model includes 33 chemical species with 41 gas-phase and 12 aqueous-phase reactions (Wang et al., 1998). For the longer-lived species ($CFCl_3$, CF_2CL_2, N_2O, CO, CO_2, NO, NO_2, N_2O_5, HNO_3, CH_4, CH_2O, SO_2, H_2SO_4, HFC, PFC, SF_6, and black carbon and organic carbon aerosols), the chemistry model includes convergence due to transport, parameterized north-south eddy transport, convective transport, and local true production and loss due to surface emissions, deposition, and chemical reaction. For the very reactive atoms (e.g., O), free radicals (e.g., OH),

and molecules (e.g., H_2O_2), concentrations are unaffected by transport due to their very short lifetimes, and only their chemical production and loss (in both the gaseous and aqueous phase) is considered. The scavenging of carbonaceous and sulfate aerosol species by precipitation is also included using a method based on a detailed 3-D climate-aerosol-chemistry model (Wang, 2004). Water vapor and air (N_2 and O_2) mass densities are computed using full continuity equations as part of the atmospheric dynamics and physics model (described above) to which the chemical model is coupled.

2.2.3. Coupling of Urban and Global Atmospheric Chemistry

The urban chemistry module was derived based on an ensemble of 24-hr-long CIT model runs and thus is processed in the IGSM with a daily time step, while the global chemistry module is run at 10-min time step for advection and scavenging, and 3-hr time step for tropospheric reactions. The two modules in the IGSM are processed separately at the beginning of each model day, supplied by emissions of nonurban and urban regions, respectively. At the end of each model day, the predicted concentrations of chemical species by the urban and global chemistry modules are then remapped based on the urban to nonurban volume ratio at each model grid. Beyond this step, the resultant concentrations at each model grid will be used as the background concentration for the next urban module prediction and also as initial values for the global chemistry module (Mayer et al., 2000).

2.3. Ocean Component

The ocean model used in the version of MESM described in this paper consists of a mixed-layer model with a horizontal resolution of 4° in latitude and 5° in longitude and a 3,000-m-deep anomaly-diffusing ocean model (ADOM) beneath. Mixed-layer depth is prescribed based on observations as a function of time and location (Hansen et al., 1983). In addition to the temperature of the mixed layer, the model also calculates the average temperature of the seasonal thermocline and the temperature at the annual maximum mixed-layer depth (Russell et al., 1985). Heat mixing into the deep ocean is parameterized by the diffusion of the difference of the temperature at the bottom of the seasonal thermocline from its value in a preindustrial climate simulation (Hansen et al., 1984; Sokolov & Stone, 1998). Since this diffusion represents a cumulative effect of heat mixing by all physical processes, the values of the diffusion coefficients are significantly larger than those used in the subgrid scale diffusion parameterizations in ocean global circulation models (OGCMs). The spatial distribution of the diffusion coefficients used in the diffusive model is based on observations of tritium mixing into the deep ocean (Hansen et al., 1988). The rate of oceanic heat uptake is varied by multiplying diffusion coefficients by the same factor in all locations.

The coupling between the atmospheric and oceanic models takes place every hour. The heat flux (*FH*) at the longitude-latitude point (*i*, *j*) is calculated as follows:

$$FH(i,j) = FHZ(j) + (\partial FHZ/\partial Tsz)\ (j) * (Ts(i,j) - Tsz(j)), \tag{2}$$

where *FHZ* (*j*) and (*∂FHZ/∂Tsz*) (*j*) are zonally averaged heat flux and its derivative with respect to surface temperature, and *Ts*(*i*, *j*) and *Tsz*(*j*) are surface temperature and its zonal mean.

Fluxes of sensible heat and latent heat are calculated by bulk formulas with turbulent exchange coefficients dependent on the Richardson number and, therefore, on surface temperature. However, to account for partial adjustment of near-surface air temperature to changes in fluxes, the derivatives of these fluxes are calculated under commonly used assumption that the exchange coefficients are fixed. A more detailed discussion of the technical issues involved in the calculations of these fluxes and their derivatives is given in Kamenkovich et al. (2002).

The mixed-layer model also includes specified vertically integrated horizontal heat transport by the deep oceans, a so-called *Q-flux*. This flux has been calculated from a simulation in which sea surface temperature and sea ice distribution were relaxed toward their present-day climatology with a relaxation coefficient of 300 W m^{-2}/K, corresponding to an *e*-folding time-scale of about 15 days for the 100-m-deep mixed layer. Relaxing SST and sea ice on such a short time scale, while being virtually identical to specifying them, avoids problems with calculating the Q-flux near the sea ice edge.

A thermodynamic ice model is used for representing sea ice. The model has two layers and computes ice concentration (the percentage of area covered by ice) and ice thickness.

An alternative version of MESM was developed by replacing the simplified ocean model with the MIT 3-D OGCM (Dutkiewicz et al., 2005). A detailed comparison of the results of simulations with the two versions of the MESM was carried out to evaluate the performance of the ADOM on different time scales by Sokolov et al. (2007). This comparison led to significant modification of the ocean carbon model originally used in ADOM (Holian et al., 2001). In the current version of the MESM, the formulation of carbonate chemistry and parameterization of air sea carbon fluxes are similar to the ones used in the MIT 3-D OGCM (Dutkiewicz et al., 2005).

Vertical and horizontal transports of the total dissolved inorganic carbon, though, are parameterized by diffusive processes. The values of the horizontal diffusion coefficients are taken from Stocker et al. (1994), and the coefficient of vertical diffusion of carbon (K_{vc}) depends on the coefficient of vertical diffusion of heat anomalies (K_v). Originally, K_{vc} was assumed to be proportional to K_v (Prinn et al., 1999; Sokolov et al., 2005). This assumption, however, does not work well in the presence of the vertical transport of carbon due to the biological pump. In the present version of MESM, K_{vc} is, therefore, defined as

$$K_{vc} = K_{vco} + rK_v \tag{3}$$

Where K_{vco} represents mixing due to the biological pump and rK_v due to physical processes. Values of K_{vco} and r are chosen based on comparison with results obtained in simulations with MIT 3-D OGCM and observations (see section 3.1). Because K_{vco} is a constant, the vertical diffusion coefficients for carbon have the same latitudinal distribution as the coefficients for heat anomalies. For simulations with different rates of oceanic uptake, the diffusion coefficients are scaled by the same factor in all locations. Therefore, rates of both heat and carbon uptake by the ocean are defined by the global mean value of the diffusion coefficient for heat. In the rest of the paper the symbol K_v is used to designate the global mean value.

Comparisons with 3-D ocean simulations have shown that the assumption that changes in ocean carbon can be simulated by the diffusive model with fixed diffusion coefficient works only for about 150 years. On longer time scales, the simplified carbon model overestimates the ocean carbon uptake. However, if K_{vc} is assumed to be time dependent, the MESM reproduces changes in ocean carbon as simulated by the 3-D OGCM on multicentury scales (Sokolov et al., 2007). Thus, for the runs discussed here, the coefficient for vertical diffusion of carbon was calculated as

$$K_{vc}(t) = (K_{vco} + rK_v)\, f(t) \tag{4}$$

Where $f(t)$ is a time-dependent function constructed based on the analyses of the depths of carbon mixing in simulations with the 3-D OGCM.

Overall results presented by Sokolov et al. (2007) show that in spite of its inability to depict feedbacks associated with the changes in the ocean circulation and a very simple parameterization of the ocean carbon cycle, the version of the MESM with the ADOM is able to reproduce the important aspects of the climate response simulated by the version with the OCGM through the 20th and 21st centuries and can be used to produce probabilistic projections of changes in many of the important climate variables, such as surface air temperature and sea level, through the end of the 21st century.

The MESM also has been shown, with an appropriate choice of the model's cloud feedback and effective diffusion coefficients, to reproduce the transient surface warming and sea level rise due to thermal expansion of the ocean as calculated in various coupled AOGCMs for 120–150-year time scales (Sokolov et al., 2003; Sokolov & Stone, 1998).

2.4. Land Component

The land component of the MESM estimates how fluxes of heat, water, carbon, and nitrogen, both within land ecosystems and between land and the atmosphere, vary across the globe over time. In addition, the land component estimates how soil moisture and the storage of carbon and nitrogen in vegetation and soils vary across the globe over time. The land fluxes and storages are estimated based on values of near-surface atmospheric states (e.g., air temperature, humidity, pressure, and wind speed) and fluxes (radiation and precipitation), as well as atmospheric chemistry (carbon dioxide and ozone), determined by the atmospheric component of the MESM, along with external data sets that prescribe the distribution of land cover and soil texture across the globe. The land component estimates of albedo, sensible heat, latent heat, evapotranspiration, and fluxes of carbon dioxide (CO_2), methane (CH_4), and nitrous oxide (N_2O) are then

used by the atmospheric component of the MESM to determine changes in atmospheric physics and chemistry. In order to assess the value of global land resources, estimates of net primary production (NPP) are used by the EPPA model in the MIT IGSM to indicate how this ecosystem service influences economic activity.

Global processes in the land component are represented with a dynamically linked set of terrestrial biogeophysical (i.e., water and energy budgets) and biogeochemical (i.e., carbon and nitrogen budgets including carbon dioxide, methane, and nitrous oxide fluxes) submodels. These biogeophysical and biogeochemical calculations are organized into a single, self-consistent framework for the global terrestrial environment and hereafter referred to as the Global Land Systems (GLS) framework (Schlosser et al., 2007). The GLS framework, employs three coupled submodels to represent the terrestrial water, energy, and ecosystem processes:

1. The CLM described by Bonan et al. (2002) calculates the global, terrestrial water and energy balances.
2. The TEM of the Marine Biological Laboratory (Felzer et al., 2004; Melillo et al., 1993, 2009; Tian et al., 1999; Xiao et al., 1997, 1998) simulates carbon and nitrogen fluxes and the storage of carbon and nitrogen in vegetation and soils including the uptake and release of CO_2 associated with NPP, decomposition, and carbon sequestration or loss.
3. The NEM described by Liu (1996) and Prinn et al. (1999) simulates CH_4 and N_2O fluxes.

Water, energy, and carbon are conserved among these submodels. The GLS is also designed to be flexible and runs either with the meridional resolution (4°) of the zonally-averaged atmospheric model within the MESM or over a latitude-longitude grid for targeted studies (e.g., 2° × 2.5° as in Gao et al., 2013 and 0.5°× 0.5° as in Melillo et al., 2009). Herein we describe the coupled configuration of the GLS used within the MESM. In this GLS configuration, a vegetation mosaic scheme has been used to represent the distribution of vegetation within a latitudinal zonal band at the same spatial resolution for all submodels. Each latitudinal band is represented with a mosaic of 35 land cover or IGSMVEG types (Schlosser et al., 2007) based on the presence or absence of a dominant tree, shrub, or grass cover, ecological region (i.e., boreal, temperate, and tropical), moisture status (upland, floodplain, or wetland), and land management (crop and pasture). The distribution of land cover types within a latitudinal zonal band is based on aggregating the area of various potential vegetation (i.e., natural vegetation in the absence of human activity) types of an underlying finer spatial resolution land cover data set (0.5^o latitude × 0.5^o longitude, Schlosser et al., 2007) found within a latitudinal zonal band. In most applications of the GLS within the MESM, the mosaic of land cover within each latitudinal zonal band has been assumed to remain constant through time such that the potential impacts of land use change on the ability of land to store carbon and nitrogen have not been considered. However, a scheme for incorporating the influence of land use change on land carbon dynamics in the GLS has been developed and applied in Eby et al. (2013) and Zickfeld et al. (2013).

To simulate the effects of climate and atmospheric chemistry conditions on land biogeophysics and biogeochemistry, the land surface estimates of solar radiation, air temperature, and atmospheric concentrations of carbon dioxide and ozone by the atmospheric component of the MESM are used directly by the GLS models for all 35 land cover types within a particular latitudinal zonal band. In contrast, zonal estimates of precipitation by the atmospheric component of MESM undergo some additional processing before being used by the GLS models. Because the emission of trace gases, such as CH_4 and N_2O, depends on episodic precipitation events and different land covers within a latitudinal band may experience very different amounts of precipitation (e.g., tropical rain forests versus arid shrub lands), a couple of procedures have been developed that provide a statistical representation of the episodic nature and spatial distribution of land precipitation. A statistical procedure based on a Poisson-based arrival process is employed to enable the episodic nature of precipitation events, with occurrence and duration resolved at an hourly time step so that this allows for soils in the land component to become wetter during some time periods to support production and emissions of trace gases than would be possible if rainfall was assumed to be distributed uniformly over the day (see Schlosser et al., 2007 for more details). An additional procedure is used within the zonal land cover mosaic framework to account for the varying degree of precipitation amounts that are received between the ocean and land as well as across the various vegetation regimes. A monthly zonal climatology is constructed from monthly observational estimates from the Global Precipitation Climatology Project Version 2 (GPCP, Adler et al., 2003), which prescribes the ratio of total land/ocean precipitation received as a fraction of the total zonal precipitation. This zonal, monthly climatology is applied at every

time step in the MESM in order to partition the simulated zonal precipitation rates over land and ocean. A similar mapping between the GPCP precipitation over the potential vegetation distribution at the 0.5° latitude × 0.5° longitude spatial resolution described above allows a further partitioning of the zonal land precipitation among all land cover types aggregated across each latitudinal band (see Schlosser et al., 2007 for more details).

For targeted studies, two approaches have been used to expand the mean latitudinal zonal estimates from the atmospheric component of the MESM to develop gridded estimates (over land) for the GLS component. In Melillo et al. (2009), the monthly zonal changes in climate are distributed to the 0.5° × 0.5° spatial resolution by applying the changes in climate estimated by the atmospheric component of the MESM to a baseline climate (Cramer & Leemans, 2001) as described previously by Xiao et al. (1997). Zonal changes in the effects of ozone on biogeochemistry have been downscaled as described by Felzer et al. (2005). In the Melillo et al. (2009) approach, general patterns of climate within a latitudinal band remain unchanged throughout the simulation. To overcome this problem, other studies (e.g., Fant et al., 2016; Gao et al., 2013; Schlosser et al., 2014) use a different approach to downscale the MESM climate based on Schlosser et al. (2013). Briefly, the method maps the zonal means of a MESM variable of interest in longitude via transformation coefficients derived from observations to obtain the baseline climatology. To account for climate change, the method tracks the characteristic patterns of response from the CMIP simulations of future climate outcomes, and through a climate-sensitivity normalization and Taylor expansion framework, the climatological patterns are augmented according to MESM's global temperature response.

Below we highlight the key features of each of the land submodels and modifications made to these submodels for their implementation in the MESM.

2.4.1. The Community Land Model

As in previous implementations of land biogeophysical and hydrologic processes within the IGSM framework, we have drawn from the CLM (Lawrence et al., 2011). The CLM has been developed from a multiinstitutional collaboration of land models and serves as the core land system model for energy, water, carbon, and nutrient cycle studies within the Community Earth System Model (Oleson et al., 2010). CLM has also been widely used and documented in land data assimilation research (e.g., Zhang et al., 2012), hydrologic studies at the global (e.g., Pu & Dickinson, 2012), regional (e.g., Swenson et al., 2012; Zampieri et al., 2012), and river basin (e.g., Vano et al., 2012) scales, as well as coupled climate prediction studies (e.g., Tseng et al., 2012; Xin et al., 2012). CLM is also benchmarked within the iLAMB framework (e.g., Randerson et al., 2009).

Within the current version of the MESM, we have employed CLM Version 3.5 that largely follows the detailed documentation provided by Oleson et al. (2010) as well as many of the features highlighted by Lawrence et al. (2011). We however have made some modifications to CLM's configuration used within the MESM. Within CLM's surface soil hydrologic formulation, infiltration of rainfall in the uppermost layer of the soil required further refinement for its implementation in MESM. In the initial testing of CLM within the MESM's zonal configuration, it was found that CLM produced excessive infiltration into the soil column. This resulted in an appreciably low bias in runoff and subsequently an excessive amount of evapotranspiration as compared to our previous versions of CLM implemented in the model and also against a multimodel consensus of estimates (Schlosser et al., 2007; see Figure 15). The algorithm that describes the infiltration rate, q_{inmax}, into the uppermost soil layer can be summarized as

$$q_{\mathrm{inmax}} \sim \left(1 - \frac{2b\psi_{\mathrm{sucsat}}}{\mathrm{d}z}\right) \times F_{\mathrm{dry}} \times K_{\mathrm{sat}} \tag{5}$$

where b is the Clapp-Hornberger parameter, ψ_{sucsat} is the soil suction from the top layer of soil, dz is the thickness of the top soil layer, F_{dry} is a dryness factor of the upper soil layer, and K_{sat} is the saturated hydraulic conductivity. This infiltration formulation closely follows that of the classic Green-Ampt formulation (1911) for *enhanced* (i.e., values greater than saturated hydraulic conductivity) infiltration rate for dry soils—and will sustain this condition for dry soils (i.e., subsaturated) in the uppermost soil layer. The inherent assumption with this formulation is that saturated and unsaturated conditions in the uppermost soil layer will occur sporadically over a large heterogeneous landscape of intermittent precipitation. However, within our zonally resolved implementation of CLM, we have removed this enhancement effect. While the MESM does resolve the temporal episodic nature of precipitation provided to the GLS (see Schlosser et al., 2007)—the spatially heterogeneous nature of these conditions is not comprehensively resolved. Therefore, we simply set the maximum infiltration rate equal to saturated hydraulic conductivity. As a result of this modification, we find that our

estimates of runoff and subsequent evapotranspiration are more aligned with present-day estimates from the more detailed models—judged commensurately on a zonally averaged basis (discussed in section 3.3).

The CLM, as well as atmospheric physics, is run at an hourly time scale in order to resolve diurnal variations in the surface energy budget and associated radiative and turbulent heat exchange as well as momentum flux between the land and atmosphere. All inputs to CLM that require a temporal sampling resolution at the time step are provided by the atmospheric model (as shown in Figure 1); CLM then calculates surface heat, water, and momentum fluxes that are passed back to the atmospheric model. The calculations of soil/vegetation water and energy states and fluxes (and corresponding storages and temperatures) are averaged and accumulated as necessary given the time steps of TEM and NEM. CLM provides estimates of soil moisture and temperature profiles, as well as evapotranspiration rates that are required inputs for the TEM and NEM components and used to estimate fluxes of CO_2, N_2O, and CH_4 between terrestrial ecosystems and the atmosphere.

2.4.2. The Terrestrial Ecosystem Model

The TEM is a process-based biogeochemistry model that uses spatially referenced information on atmospheric chemistry, climate, elevation, soil texture, and land cover to estimate monthly fluxes and pool sizes of carbon, nitrogen, and water among vegetation, soils, and the atmosphere. The TEM is well documented and has been used to examine patterns of land carbon dynamics across the globe including how they are influenced by multiple factors such as CO_2 fertilization, ozone pollution, climate change and variability, and land use change, (Felzer et al., 2004, 2005; Galford et al., 2010, 2011; Kicklighter et al., 2012, 2014; Melillo et al., 2009, 2016; Reilly et al., 2007, 2012; Sokolov et al., 2008).

In TEM, the uptake of atmospheric carbon dioxide by vegetation, also known as gross primary production or GPP, is dependent upon photosynthetically active radiation (PAR), leaf phenology, air temperature, evapotranspiration rates, atmospheric concentrations of carbon dioxide and ozone, the availability of inorganic nitrogen in the soil, and the ratio of carbon to nitrogen (C:N) of new plant biomass (Felzer et al., 2004; McGuire et al., 1997; Raich et al., 1991; Tian et al., 1999). Carbon dioxide is released back to the atmosphere from terrestrial ecosystems as a result of the autotrophic respiration (R_A) of plants and the heterotrophic respiration (R_H) associated with the decomposition of detritus. NPP, which is an important source of food and fiber for humans and other organisms on Earth, is the net uptake of atmospheric carbon dioxide by plants and is calculated as the difference between GPP and R_A. Heterotrophic respiration depends upon the amount of soil organic matter, the C:N ratio of the soil organic matter, air temperature, and soil moisture (McGuire et al., 1997; Raich et al., 1991; Tian et al., 1999). Within an ecosystem, carbon may be stored either in vegetation biomass or in detritus (i.e., litter, standing dead, and soil organic matter). In TEM, the carbon in vegetation biomass and detritus are each represented by a single pool. The transfer of carbon between these two pools is represented by litterfall carbon (L_C), which is calculated as a proportion of vegetation carbon. Changes in vegetation carbon (ΔC_{Veg}, also known as biomass increment), detritus (ΔC_{Soil}), and terrestrial carbon (ΔC_{Tot}) are then determined as a linear combination of these fluxes:

$$\Delta C_{Veg} = GPP – R_A – L_C \tag{6}$$

$$\Delta C_{Soil} = L_C - R_H \tag{7}$$

$$\Delta C_{Tot} = \Delta C_{Veg} + \Delta C_{Soil} = NPP - R_H = GPP - R_A - R_H \tag{8}$$

Carbon sequestration in undisturbed terrestrial ecosystems can be estimated by the GLS either as the sum of the estimated changes in carbon in vegetation and detritus or by the difference between NPP and R_H (equation (8)) which is also known as net ecosystem production or NEP.

An important feature of TEM is that the model simulates the influence of terrestrial nitrogen dynamics on terrestrial carbon dynamics. First, the uptake of carbon dioxide by plants is assumed by TEM to be limited by nitrogen availability in most land ecosystems on Earth. Tropical forests are the only exceptions, where nitrogen availability is not assumed to limit GPP under contemporary conditions. The effect of nitrogen limitation on GPP is determined by first calculating GPP_C assuming no nitrogen limitation:

$$GPP_C = \mathrm{f}\,(CO_2, ET)\,\mathrm{f}(PAR)\,\mathrm{f}(CANOPY)\,\mathrm{f}(LEAF)\,\mathrm{f}(T)\,\mathrm{f}(O_3, ET) \tag{9}$$

where CO_2 is atmospheric CO_2 concentration, ET is evapotranspiration, *PAR* is photosynthetically active radiation, *CANOPY* is the relative state of a vegetation canopy recovering from a disturbance as compared

Table 1
Percentiles for Climate Parameters

	Climate sensitivity K	Square root of diffusion coefficient cm/s$^{1/2}$	Radiative forcing due to aerosol radiation interaction averaged for 2001–2010 W/m^2
5%	2.4	0.9	−0.47
50%	3.2	1.8	−0.24
95%	4.6	3.7	−0.05

to the canopy state of a mature, undisturbed stand, *LEAF* is the monthly leaf area relative to the maximum leaf area of a stand, *T* is air temperature, and O_3 is atmospheric ozone concentration. The influence of atmospheric CO_2 and O_3 concentrations on GPP depends on the status of vegetation stomates, which close during drier conditions (i.e., low ET) to reduce the uptake of CO_2 or O_3 and open during wetter conditions (i.e., high ET). Details of equation (9) have been described elsewhere (e.g., Felzer et al., 2004; McGuire et al., 1992, 1995, 1997; Pan et al., 1998; Raich et al., 1991; Tian et al., 1999).

If GPP is limited by nitrogen availability, GPP_N is then calculated based on the effects of nitrogen supply on net primary production (NPP_N):

$$NPP_N = P_{CN}\,(NUPTAKE + NMOBIL) \tag{10}$$

$$GPP_N = NPP_N + R_A \tag{11}$$

where P_{CN} is the carbon to nitrogen ratio (C:N) of newly produced plant tissue, *NUPTAKE* is the amount of inorganic nitrogen acquired by plants from the soil and *NMOBIL* is the amount of vegetation labile nitrogen mobilized during a particular month (McGuire et al., 1997; Pan et al., 1998; Tian et al., 1999). Similar to GPP_C, NUPTAKE also depends on local environmental conditions (Felzer et al., 2004; McGuire et al., 1992; Raich et al., 1991):

$$NUPTAKE = \mathrm{f}(N_{AVL}, H_2O)\,\mathrm{f}(CANOPY)\,\mathrm{f}(T)\,\mathrm{f}(O_3, ET)$$

where N_{AVL} is soil available nitrogen and H_2O is soil moisture. Monthly GPP is then determined as follows:

$$GPP = \min\,(GPP_C, GPP_N) \tag{12}$$

In TEM, the uptake of atmospheric CO_2 by plants is assumed to follow Michaelis–Menten kinetics such that the effect of atmospheric CO_2 at time *t* as modified by *ET* on the assimilation of CO_2 by plants is parameterized as follows:

$$\mathrm{f}(CO_2(t)) = (C_{max}\,CO_2(t))/(kc + CO_2(t)) \tag{13}$$

where C_{max} is the maximum rate of C assimilation, and *kc* is the CO_2 concentration at which C assimilation proceeds at one-half of its maximum rate (i.e., C_{max}). Because the response of carbon uptake by plants to atmospheric CO_2 concentrations is uncertain (Sokolov et al., 2009), we examine the influence of this uncertainty on terrestrial carbon dynamics by adjusting the value of *kc* in our uncertainty analyses.

The NEM has been embedded within the TEM infrastructure as described in Schlosser et al. (2007) to estimate CH_4 and N_2O fluxes, which are not estimated by TEM. As such, the CH_4 and N_2O flux estimates by NEM are directly based on monthly TEM estimates of soil organic carbon. Although the simulated carbon and nitrogen dynamics of NEM are still mostly separated from those in TEM, the embedded NEM provides a platform for

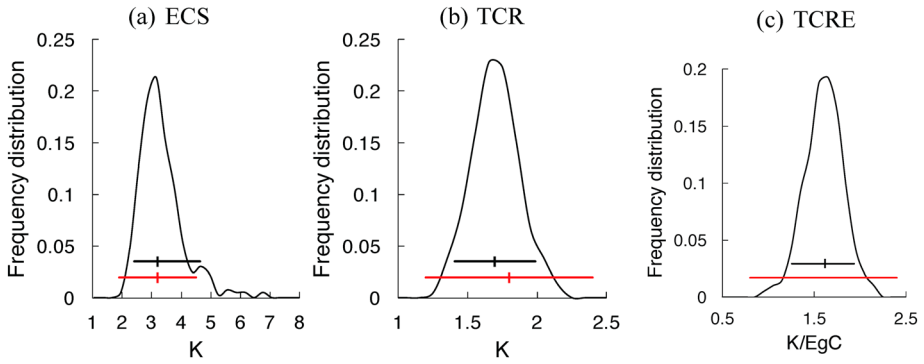

Figure 2. Frequency distribution of (a) ECS, (b) TCR, and (c) TCRE. Vertical line shows median value, and horizontal bar shows 90% probability interval. Red line CMIP5 estimate, from Table 9.5 of IPCC (2013) for TCR and from Gillet et al. (2013) for TCRE. ECS = equilibrium climate sensitivity; TCR = transient climate response; TCRE = transient climate response to cumulative carbon emission.

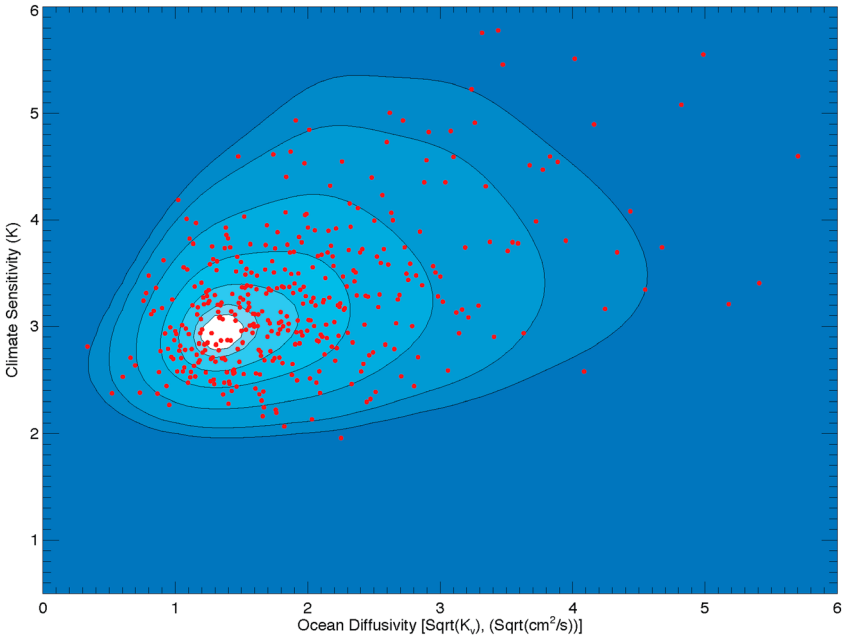

Figure 3. Distribution of climate sensitivity and the rate of ocean heat uptake (square root of vertical diffusion coefficient). Red dots show values of CS and SQRT(Kv) for 400 samples.The contour lines are for the 5th, 10th, 25th, 50th, 75th, 90th, and 95th percentiles.

improving the linkages between the two biogeochemistry models. For example, NEM estimates of CH_4 emissions diminish the stock of soil organic carbon and associated CO_2 emissions estimated by TEM. The embedded NEM allows simulation of daily CH_4 and N_2O emissions based on monthly estimates of soil organic carbon by TEM combined with the CLM estimates of daily soil temperatures, daily and hourly soil moistures, hourly rainfall intensities, and storm durations. CLM also provides all data on soil properties required by TEM/NEM. Fluxes of CO_2, CH_4, and N_2O are passed to atmospheric model and are used in calculations of the corresponding gases by the atmospheric chemistry submodel.

3. Model Evaluation

As mentioned earlier, the MESM can be run either in concentration-driven or emissions-driven mode. In historical simulations, the MESM is forced by the prescribed changes in greenhouse gases and ozone concentrations, aerosols, and solar irradiance. Greenhouse gas concentrations and stratospheric aerosols from volcanic eruptions are taken from the NASA GISS modeling group forcing suite. Miller et al. (2014) describe the methods for updating the greenhouse gas concentrations from Hansen et al. (2007) and the volcanic aerosol optical depths from Sato et al. (1993). Sulfate aerosol loadings are from Smith et al. (2011) extended by Klimont et al. (2013), solar irradiance is from the Kopp and Lean (2011) data set, and ozone concentrations are from the SPARC data set used in the CMIP5 experiments (Cionni et al., 2011). In future climate simulations, the MESM is driven by anthropogenic emissions of different gases produced by the MIT EPPA model (Paltsev et al., 2005).

Table 2
Median Values and 90% Probability Intervals for Surface Air Temperature Anomaly Relative to 1986–2005 Mean in Simulations With RCP8.5 Scenario

	CMIP5	MESM
2046–2065	2.0 (1.4, 2.6)	1.7 (1.3,2.0)
2081–2100	3.7 (2.6, 4.8)	3.1 (2.6,3.8)
2181–2200	6.5 (3.3, 9.8)	7.0 (5.7,8.9)
2281–2300	7.8 (3.0, 12.6)	8.9 (6.9,11.0)

Note. CMIP5 results are from Table 12.2 of IPCC (2013). RCP = Representative Concentration Pathways; CMIP5 = Coupled Model Intercomparison Project Phase 5; MESM = MIT Earth System Model of intermediate complexity; MIT = Massachusetts Institute of Technology.

3.1. Distribution of Climate Parameters and Characteristics Describing Model Response to External Forcing

To determine climate model parameters that produce changes in surface air and ocean temperatures consistent with available observations, 1,800 historical simulations from 1861 to 2010 were carried out changing climate sensitivity, the rate of ocean heat uptake, and the strength of aerosol forcing over wide ranges. Probability distributions for climate parameters were constructed using the methodology described in Forest et al. (2002, 2008) and Libardoni and Forest (2011, 2013). Detailed descriptions

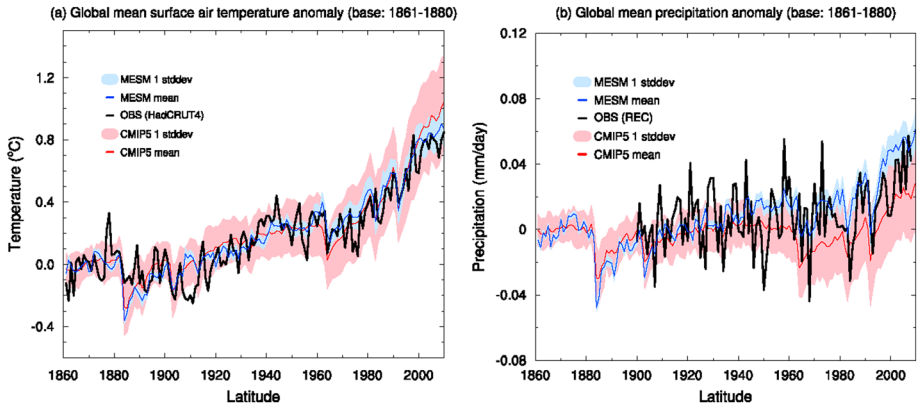

Figure 4. Time series of global mean surface air temperature and precipitation relative to 1861–1880 mean. The simulations with the MESM are shown in blue (ensemble mean and 1 standard deviation in shading) and the simulations from the CMIP5 MME are shown in red (MME mean and 1 standard deviation in shading). After 2006, simulations under the RCP8.5 are used. Observations are shown in black lines, namely the HadCRUT4 (Morice et al., 2012) and global reconstructed precipitation (REC) data (Smith et al., 2012) for temperature and precipitation, respectively. MESM = MIT Earth System Model of intermediate complexity; MIT = Massachusetts Institute of Technology; CMIP5 = Coupled Model Intercomparison Project Phase 5.

of the distributions obtained using different observational data sets, different estimates of natural variability, and other assumptions are given in Libardoni (2017). Below we describe our final distributions and present the results of simulations with the set of climate parameters sampled from it. This distribution is derived using multiple data sets for changes in surface temperature from 1905 to 2010 and in ocean heat content from 1990 to 2010. Individual distributions were merged across all-surface data sets to produce the final distribution. Estimates of natural variability from all CMIP5 models were used to estimate the noise-covariance matrix.

Table 1 shows medians and 90% probability intervals for model climate parameters from the distribution used in this paper. The median values for equilibrium climate sensitivity (ECS, Figure 2a) is rather close to the median climate sensitivity of CMIP5 AOGCMs (3.2 K), while the 90% probability interval is shifted toward higher values compared with the CMIP5 models (1.9 to 4.5 K).

To assess uncertainty in the transient climate response (TCR, i.e., temperature change in the time of CO_2 doubling), we carried out a set of climate simulations with a 1% per year increase of CO_2 concentration using 400 samples of climate parameters. To estimate uncertainty in the carbon cycle, we calculated carbon uptake by the ocean and terrestrial ecosystems in these simulations. As discussed above, the vertical diffusion

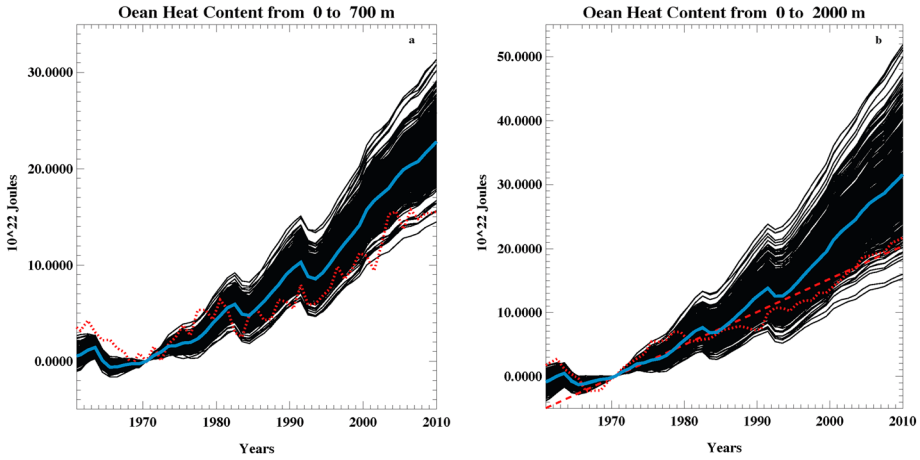

Figure 5. Changes in ocean heat content relative to 1971 in the top 700 m (a) and top 2000 m (b). Black lines are ensemble of MESM simulations. Blue lines are ensemble means. Red lines are observations from Levitus et al. (2012). MESM = MIT Earth System Model of intermediate complexity; MIT = Massachusetts Institute of Technology.

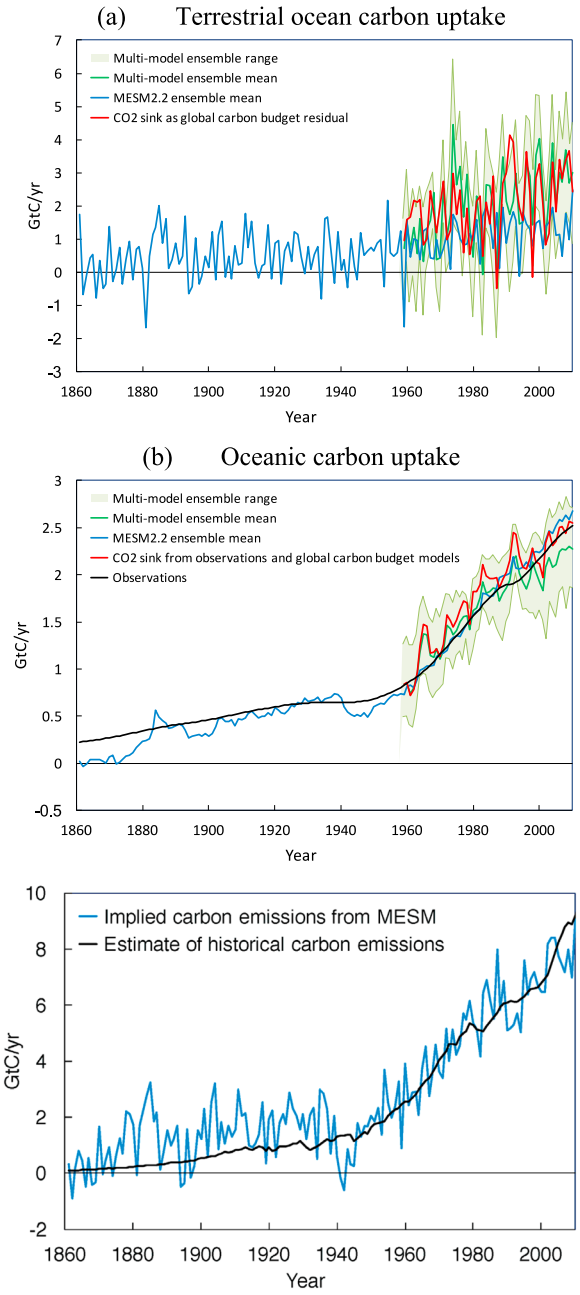

Figure 6. (a) Terrestrial, (b) oceanic carbon uptake, and (c) implied carbon emissions. Data for comparison are from Le Quere et al. (2016). MESM = MIT Earth System Model of intermediate complexity; MIT = Massachusetts Institute of Technology.

coefficient for carbon depends on the vertical diffusion coefficient for heat anomalies. As a result, uncertainty in oceanic carbon uptake is defined by the uncertainty in the heat uptake. In all simulations described in this paper we used K_{vco} = 1 cm^2/s and r = 0.52 (equation (3)). Uncertainty in the terrestrial carbon uptake was taken into account by varying the half-saturation constant, *kc* (equation (13)). The results of CO_2 enrichment studies suggest that plant growth could increase by 24%–54% in response to doubled CO_2 given adequate nutrients and water (Curtis & Wang, 1998; Gunderson & Wullschleger, 1994; McGuire et al., 1992; Norby et al., 1999, 2005; Raich et al., 1991). In the stand-alone TEM, a value of 400 ppmv CO_2 is chosen for the half-saturation constant, *kc,* so that f(CO_2(t)) increases by 37% for a doubling of atmospheric CO_2 (e.g., McGuire et al., 1997; Pan et al., 1998). A 24% and 54% response to doubled CO_2 would correspond to *kc* values of 215 and 800 ppmv CO_2, respectively. Changes in *kc* affect strengths of both carbon-concentration and carbon-climate feedbacks (Sokolov et al., 2008). It should be noted that, because TEM takes into account nitrogen limitation on carbon uptake, terrestrial carbon feedback in our model is weaker than in models which do not consider impact of nitrogen availability (Eby et al., 2013; Plattner et al., 2008; Sokolov et al., 2008).

Based on a comparison of the TEM version implemented in the MESM with other terrestrial carbon models (Sokolov et al., 2008) and results from stand-alone TEM simulations, different values of *kc* are used for nitrogen-limited and nonlimited ecosystems. In the simulations discussed below, the value of *kc* was varied from 200 to 800 ppmv CO_2 for nitrogen-limited ecosystems and from 75 to 300 ppmv CO_2 for ecosystems with no nitrogen limitations.

Total carbon uptake can be estimated from available data on carbon emissions and observed CO_2 concentrations and is less uncertain than carbon uptake by the ocean and carbon uptake by terrestrial ecosystem separately. To take this into account, low values of K_v (small carbon uptake by the ocean) are coupled with high values of *kc* (large terrestrial carbon uptake).

A dependency between the diffusion coefficients for heat and carbon imposes a correlation between heat and carbon uptake which, in turn, may lead to a correlation between, for example, TCR and the airborne fraction of carbon emissions. The latter will be weakened by the anticorrelation between oceanic and terrestrial carbon uptakes. We discuss the uncertainty in the implied carbon emissions and their airborne fraction in the next section.

Figure 2b shows frequency distributions for TCR from 400 simulations. The median value for TCR (1.7 K) is close to that for CMIP5 model (1.8 K), while the 90% probability interval (1.4–2.0 K) is significantly narrower than estimates based on CMIP5 models (1.2–2.4 K). The relatively small range of TCR in our simulations is explained in part by the correlation between climate sensitivity and the rate of oceanic heat uptake imposed by observations (Figure 3). Another characteristic often used to describe transient model response to forcing is a *realized warming* defined as a ratio of TCR to equilibrium climate sensitivity (ECS, Millar et al., 2015). In our simulations, this characteristic ranges from 0.35 to 0.66 (90% interval) with a median value of 0.54. The fact that these values are smaller than corresponding values for CMIP5 model (0.46–0.72 and 0.58) indicates that the rate of oceanic heat uptake in CMIP5 models is most likely smaller than in our simulations.

The transient climate response to cumulative carbon emission (TCRE), is defined as the ratio of surface warming to cumulative implied carbon emissions at the time of CO_2 doubling from simulations with a 1% per year increase in CO_2 concentrations (Matthews et al., 2009). Values of TCRE in MESM simulations vary

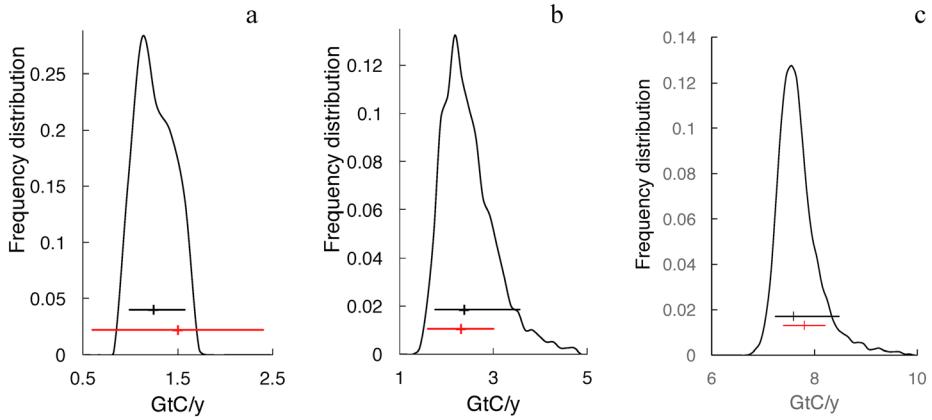

Figure 7. Frequency distribution of (a) terrestrial, (b) oceanic carbon uptake, and (c) implied carbon emissions averaged over years 2000–2009. The black line represents the 90% interval from the MESM ensemble. The red line represents the AR5 estimate (Table 6.1 in IPCC, 2013) for uptakes and data from Le Quéré et al. (2018) for emissions. MESM = MIT Earth System Model of intermediate complexity; MIT = Massachusetts Institute of Technology.

(90% range) from 1.2 to 1.9 K/EgC (Figure 2c). According to Gillet et al. (2013), a similar range for CMIP5 models is 0.8–2.4 K/EgC. At the same time, observationally constrained range, obtained using CMIP5 simulations and observed temperature to 2010, is 0.7–2.0 K/EgC (Gillet et al., 2013).

It should be noted that ranges of ECS, TCR, and TCRE shown on Figure 2 are not the full ranges which can be spanned with MESM. In historical simulations used to obtain climate parameter distributions (Libardoni, 2017), ECS was varied from 0.5 to 9.5 °C and the diffusion coefficient from 0 to 64 cm^2/s. The TCR range corresponding to these ranges in model parameters is 0.4–4.9 °C. The ECS distribution in Figure 2a is the posterior distribution obtained by Libardoni (2017). Distributions for TRC and TCRE are distributions obtained using model parameters sampled from distribution from Libardoni (2017). As a result, these are observationally constrained distributions.

To evaluate the uncertainty in long-term climate system response implied by the distribution of climate parameters described above, we carried out an ensemble of simulations using RCP8.5 GHGs concentrations. Comparison between the results from this ensemble and those from the multimodel CMIP5 ensemble are presented in Table 2. The MESM simulates less surface warming during the 21st century than the CMIP5 ensemble which, in part, may be explained by the fact that most of CMIP5 models overestimate warming in the first decade of the 21st century. At the same time, MESM simulates stronger temperature increase during 22nd and 23rd centuries than the CMIP5 models. It should be kept in mind that from the 39 CMIP5 models that ran the RCP8.5 simulation, only 12 were run beyond 2100. As can be seen on Figure 12.5 of IPCC (2013), the multi-model mean surface warming in 2100 is smaller for these 12 models than for all 39 models. The use of a different number of CMPI5 models in different simulations somewhat complicates the comparison between CMIP5 and MESM results. The estimates for ECS and TCR, shown above, are from simulations with 23 and 30 CMIP5 models, respectively (Table 9.5 in IPCC, 2013). The TCRE estimates are based on the results of 15 CMIP5 ESMs (Gillet et al., 2013).

3.2. Historical Climate Change

To assess the quality of the method used to obtain the probability distributions for climate model parameters, we carried out a 400-member ensemble of simulations over the 1861–2010 period using Latin hypercube sampling of the probability distributions. The model ensemble reproduces the observed changes in surface air temperature very well (Figure 4a). Temperature averaged over the first decade of the 21st century increases in our simulations relative to the 1861–1880 mean between 0.67 and 1 K (90% probability interval) with a mean value of 0.835 K. Corresponding values for the decade of 1986–2005 are 0.53 to 0.85 K and 0.69 K. Similar to the TCR, the range of temperature change simulated by the MESM ensemble is significantly narrower than the one produced by the CMIP5 models. The MESM ensemble mean agrees better with the observation than the CMIP5 mean, especially after year 2000, when the CMIP5 models overestimate observed warming. If averages for observed and simulated

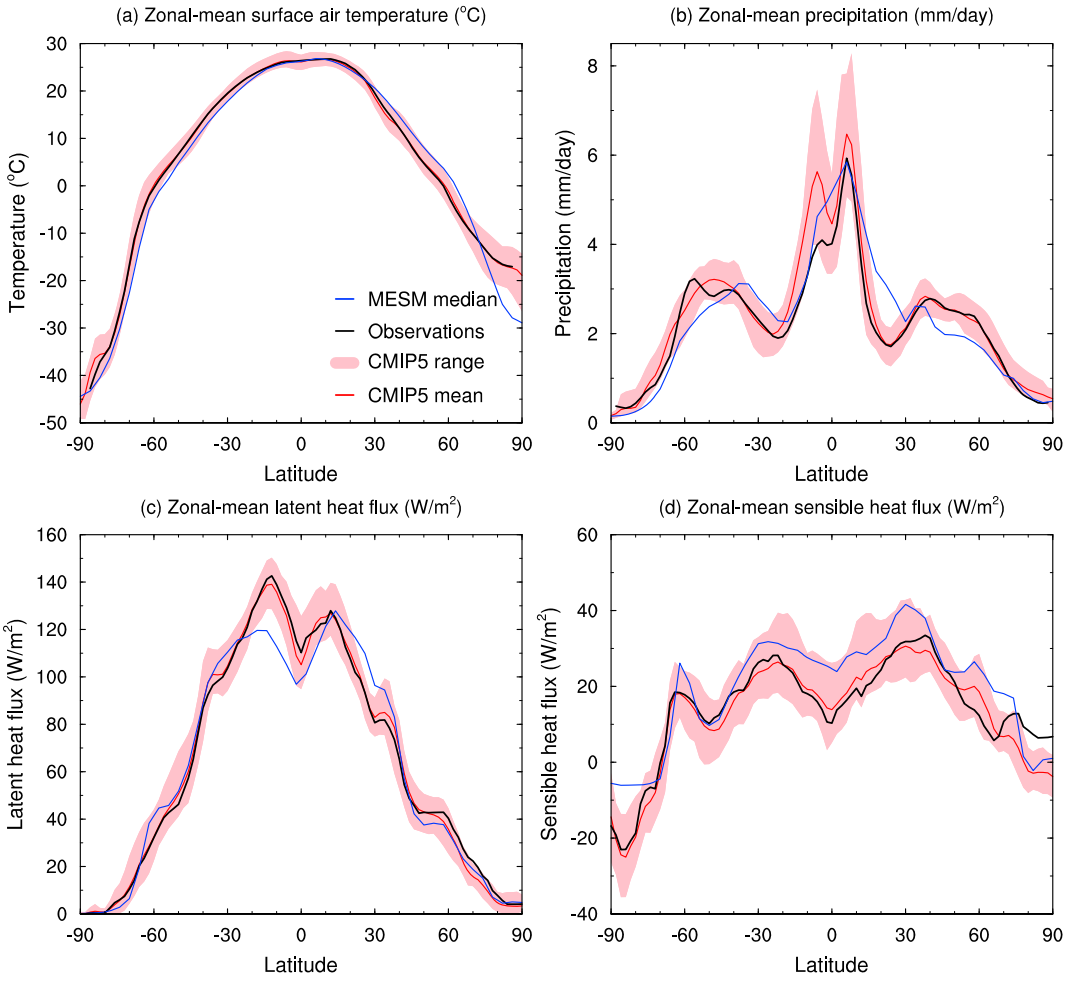

Figure 8. Zonal distribution of (a) surface air temperature (°C), (b) precipitation (mm/day), (c) surface latent heat flux (W/m^2), and (d) surface sensible heat flux (W/m^2) averaged over the 1991–2010 period. The MESM simulation with the median values of climate parameters (climate sensitivity, ocean heat uptake rate, and net aerosol forcing) is shown in blue. Simulations from the CMIP5 MME are shown in red (MME mean and full range in shading). After 2006, simulations under the RCP8.5 are used. Observations are shown in black lines, namely the HadCRUT4 (Morice et al., 2012), GPCP v2.3 (Adler et al., 2003), and MERRA2 (Gelaro et al., 2017) for temperature, precipitation, and the heat fluxes, respectively. MESM = MIT Earth System Model of intermediate complexity; MIT = Massachusetts Institute of Technology; CMIP5 = Coupled Model Intercomparison Project Phase 5; RCP8.5 = Representative Concentration Pathways 8.5; GPCP v.2.3= Global Precipitation Climatology Project Version 2.3; MERRA2 = Modern-Era Retrospective Analysis for Research and Applications, Version 2.

temperature are calculated using the same methodology, then it was shown that the agreement between CMIP5 models and observations became better (e.g., Cowtan et al., 2015; Richardson et al., 2016). Good agreement between the MESM results and observations is explained by the fact that the observations were used to create the distributions for the climate parameters. As shown by Libardoni (2017), the MESM also overestimates warming during the first decade of the 21st century for climate parameter distributions based on data through 2000 only.

Changes in global mean precipitation simulated by the MESM (Figure 4b) also agree well with observations, especially the increase in the last 50 years. Again, the MESM ensemble mean agrees better with the observations than the CMIP5 models. However, inter-annual variability simulated by MESM is much smaller than observed.

The MESM simulates a larger increase in the ocean heat content both in the top 700 m and 2,000 m (Figure 5) compared with observations and the CMIP5 models (Figure 9.17 in IPCC, 2013). At the same time, sea level increases due to thermal expansion at the rate of 0.85 (0.625–1.4) mm/year between 1971 and 2010 and at

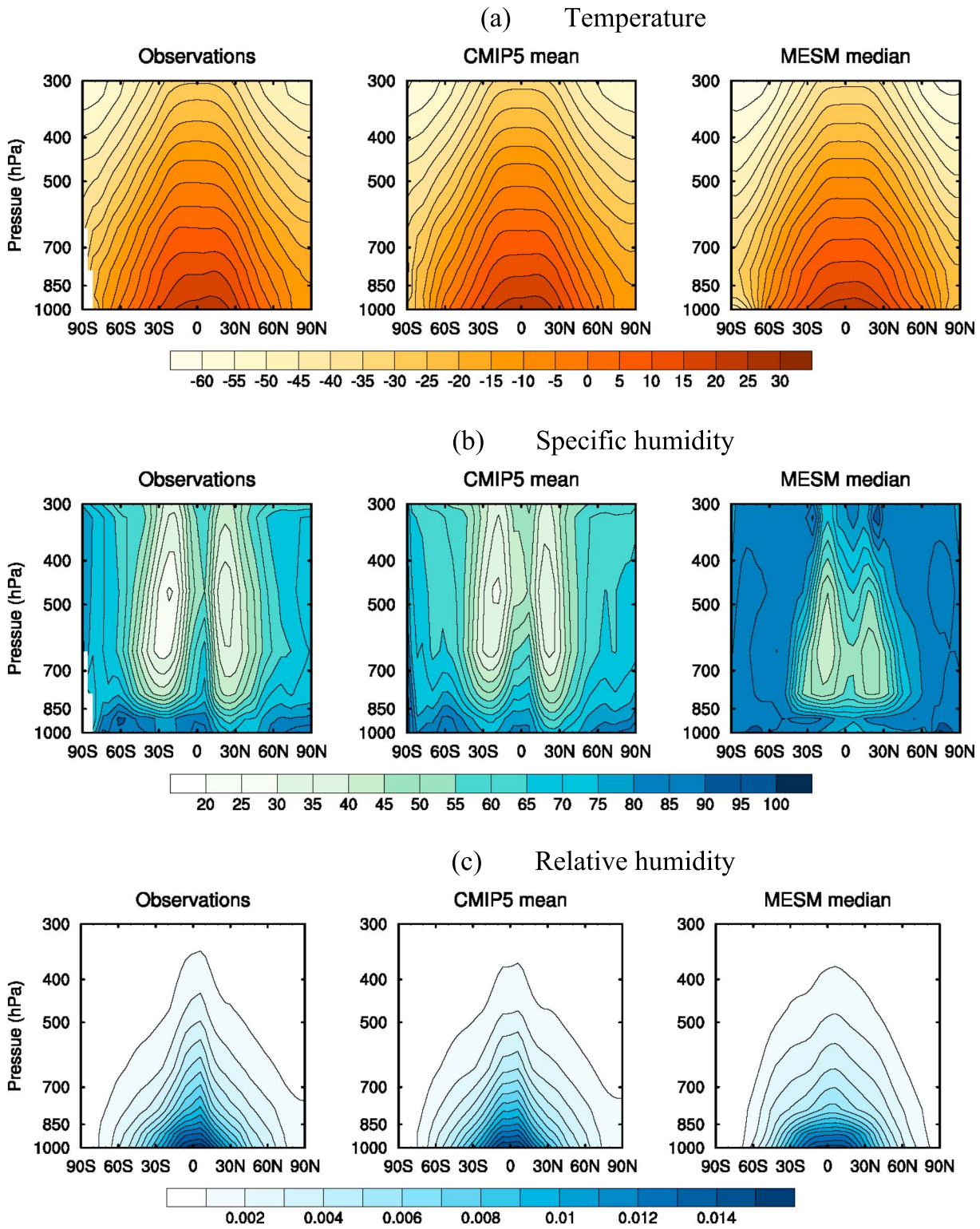

Figure 9. Latitude-height cross section of (a) temperature (°C), (b) specific humidity (kg/kg), and (c) relative humidity (%) averaged over the 1991–2010 period. Observations from MERRA2 (Gelaro et al., 2017) are shown on the left panels, the CMIP5 multimodel ensemble mean is shown in the middle panels, and the MESM simulation with the median values of climate parameters (climate sensitivity, ocean heat uptake rate, and net aerosol forcing) is shown in the right panels. After 2006, CMIP5 simulations under the RCP8.5 are used. MERRA2 = Modern-Era Retrospective Analysis for Research and Applications, Version 2; CMIP5 = Coupled Model Intercomparison Project Phase 5; MESM = MIT Earth System Model of intermediate complexity; MIT = Massachusetts Institute of Technology;.RCP8.5 = Representative Concentration Pathways 8.5.

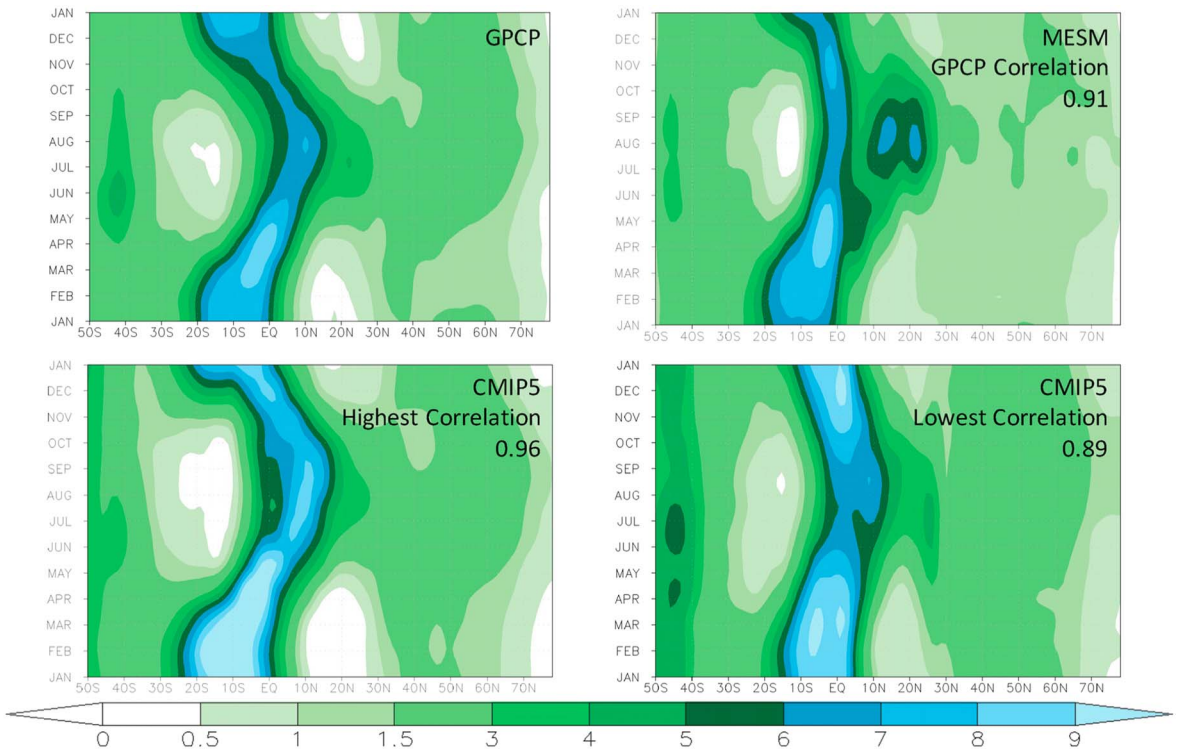

Figure 10. Month versus latitude profiles of land-only precipitation (mm/day) given by observations from the GPCP (upper left); MESM (upper right), as well as two simulations from the CMIP5 (lower panels). In each of the model-result panels, the correlation of its month versus latitude profile to that of GPCP is given. The CMIP5 results show two models that were found to have the highest (lower left) and lowest (lower right) pattern correlation with the GPCP observations. GPCP = Global Precipitation Climatology Project; MESM = MIT Earth System Model of intermediate complexity; MIT = Massachusetts Institute of Technology; CMIP5 = Coupled Model Intercomparison Project Phase 5.

the rate of 1.2 (0.96–1.6) mm/year between 1993 and 2010. These trends are not too different from the estimates given by IPCC, 0.8(0.5 to1.1) mm/year and 1.1(0.8 to 1.4) mm/year, respectively (Table 3.1 in IPCC, 2013).

While the TEM calculates carbon fluxes for natural ecosystems using potential land cover distribution, CO_2 emissions associated with agricultural activity are provided by the EPPA model in the emissions-driven simulations. Nonetheless, terrestrial carbon uptake estimates generally fall within the range of the Global Carbon Project multimodel analysis (Le Quere et al., 2016) while being smaller than the Global Carbon Project's estimate obtained as the residual from the global carbon budget (Figure 6a). The median value of the terrestrial carbon uptake averaged over 2000–2009 (Figure 7a) is about 0.25 GtC/year smaller than the best estimate provided by IPCC (2013). This can be partially attributed to the fact that nitrogen deposition is not taken into account. Simulated uncertainties in terrestrial uptake are also smaller than those suggested by IPCC (2013). Ensemble mean carbon uptake by the ocean (Figure 6b) agrees very well with data from the Global Carbon Project (Le Quere et al., 2016). However, the range on oceanic carbon obtained in our simulations is slightly shifted toward high values compare to IPCC estimate (Figure 7b). Implied carbon emissions agree well with historical estimates from global carbon project (Le Quéré et al., 2018) during the second half of the 20th century (Figure 6c). In the first decade of the 21st century, implied MESM emissions are 0.2 GtC/year smaller than estimated by Le Quéré et al. (2018) (Figure 7c). At the same time, estimates of the airborne fraction of carbon emissions agree well with results of the CMIP5 model reported by Jones et al. (2013). Mean value of the airborne fraction in the MESM ensemble is 0.5 with a 90% probability range of 0.46–0.53. Mean value for the CMIP5 models is 0.52 with 70% of the model estimates (9 of 13) falling in the 0.45–0.55 range.

3.3. Present-Day Climate

3.3.1. Meteorological Variables

In this section, we compare annual mean data from our simulations averaged over the 1991–2010 period with available observations and results from CMIP5 (Taylor et al., 2012) simulations. While estimating

Table 3
Summary Statistics for Simulated Fluxes in the Land Water/Energy Cycles

	Evaluation with GPCP observed precipitation (1981–2005)		Comparison to MESM simulation (1981–2005)			
			Evaporation		Runoff	
Model	Correlation	Bias	Correlation	Bias	Correlation	Bias
MESM	0.91	−0.04				
CMIP5 Average	0.94	0.03	0.89	0.57	0.70	0.20
ACCESS1–3	0.95	0.48	0.85	0.69	N/A	
CanESM2	0.94	−0.50	0.90	−0.02	0.62	−0.43
CCSM4	0.95	0.32	0.90	0.69	0.72	−0.19
CNRM-CM5–2	0.93	0.10	0.90	0.50	0.58	−0.14
CSIRO-Mk3–6-0	0.91	−0.27	0.86	0.01	0.70	−0.24
FGOALS-g2	0.94	0.07	0.87	0.49	0.73	−0.07
GFDL-ESM	0.96	0.32	0.90	0.61	0.77	−0.15
GISS-E2-H	0.89	0.47	0.83	0.73	0.66	−0.35
HadGEM2/CM3	0.93	0.01	0.85	0.48	0.57	−0.21
IPSL-CM5A-MR	0.90	−0.29	0.84	0.27	0.67	−0.19
MIROC5	0.95	0.54	0.86	0.73	0.72	−0.07
MPI-ESM-MR	0.90	−0.25	0.81	0.23	0.50	−0.45
MRI-CGCM3	0.91	0.11	0.83	0.35	0.73	−0.03
NorESM1-ME	0.95	0.20	0.87	0.74	0.70	−0.28

Note. Shown are correlations and bias (mm/day) of precipitation, evapotranspiration, and runoff. The correlations are performed on the month versus latitude projections shown and discussed. For precipitation, all model simulations are judged against the GPCP observations. For evaporation and runoff, these metrics are performed for the CMIP5 models against the MESM result in order to convey the degree of consistency between the more complex CMIP models to MESM's intermediate complexity. Note that the ACCESS1–3 outputs of total runoff were not made publicly available (N/A). Sign convention for bias is positive when CMIP5 value exceeds MESM or model exceeds observation. GPCP = Global Precipitation Climatology Project; MESM = = MIT Earth System Model of intermediate complexity; CMIP5 = Coupled Model Intercomparison Project Phase 5; CCSM = Community Climate System Model; GISS = Goddard Institute for Space Studies.

changes in global mean temperature and precipitation really well (Figure 4), the MESM simulations have some difficulties matching the observed zonal distributions for present-day climate. The MESM estimates somewhat lower temperature in the Southern Hemisphere and noticeably higher temperature in the midlatitudes in the Northern Hemisphere (Figure 8a). The MESM also overestimates precipitation in the descending branch of mean meridional circulation in the Northern Hemisphere and underestimates precipitation in the midlatitude storm track regions (Figure 8b), which shows the limitations of using a zonal-mean atmosphere model. The MESM realistically simulates the general characteristics of both surface latent and sensible heat fluxes (Figures 8c and 8d) and their latitudinal distributions fit within the range of the CMIP5 state-of-the-art climate models except over a few latitude bands, specifically 20°S–equator and 20°N–35°N for latent heat flux and 90°S–80°S and 65°–75°N for sensible heat flux. Latitude height cross sections of annual mean temperature, specific humidity, and relative humidity are shown in Figure 9. The MESM is able to reproduce the overall latitudinal and vertical distributions of temperature and humidity generally well despite a cold bias in the polar regions, the maximum specific humidity in the equatorial regions not extending into the upper troposphere and high relative humidity values, especially in the midlatitudes and polar regions.

3.3.2. Terrestrial Water Cycles

Global precipitation over land constitutes a substantial segment of the terrestrial water cycle and strongly influences the carbon and nutrient cycles tracked by TEM. As such, we compared MESM to the observationally based estimate from the GPCP (Adler et al., 2003; 2012). We find that the MESM estimate of land-only precipitation depicts the key seasonal and zonal attributes to a level that is very comparable with the CMIP5 models (Figure 10). At the global scale (Table 3), the MESM is closely aligned with the GPCP estimate and also is centrally placed across the estimates of the CMIP5 models (equally biased high and low across each of these climate models). Some notable discrepancies are that land-only precipitation is biased low during the NH summertime midlatitude regions. This deficiency in summertime precipitation contributes correspondingly to slightly lower evapotranspiration rates compared to most of the CMIP5 models (Figure 11 and Table 3),

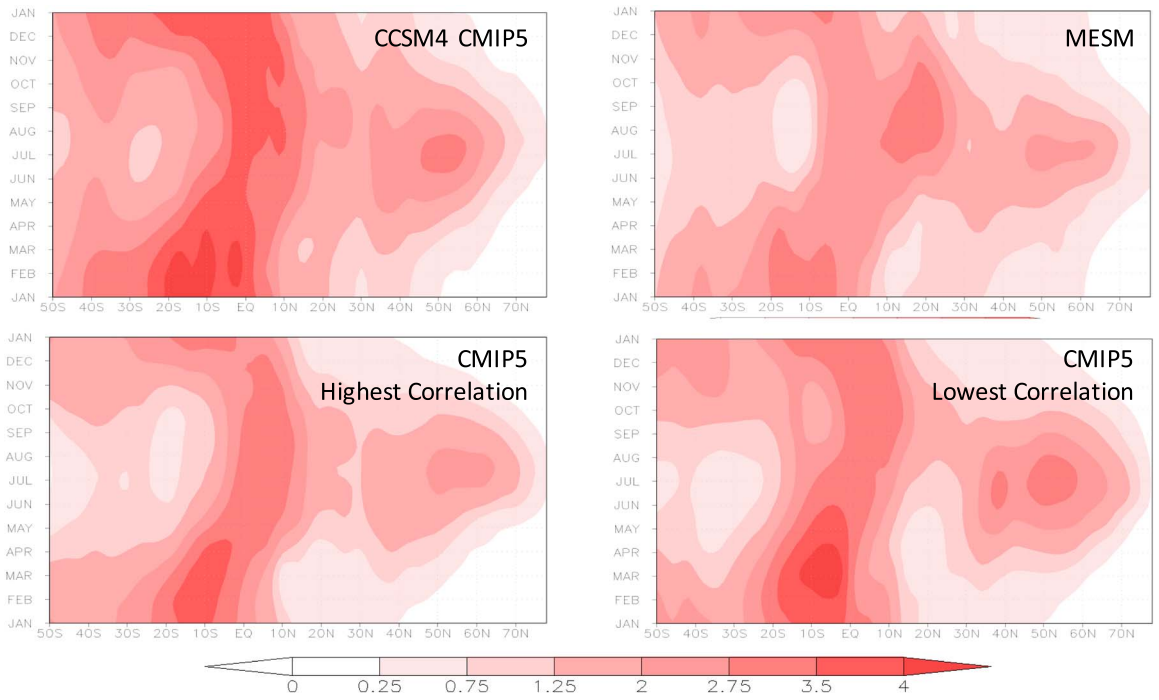

Figure 11. Month versus latitude profiles of evapotranspiration (mm/day) from the MESM (upper right panel), as well as two simulations from the CMIP5 (lower panels). The CMIP5 results show the two models with the highest (lower left) and lowest (lower right) pattern correlation with MESM. Also shown is the simulation from CCSM4 (upper left) panel. CCSM4 and the GLS component of MESM both use the CLM for the calculation of the land-surface water and energy budgets. MESM = MIT Earth System Model of intermediate complexity; MIT = Massachusetts Institute of Technology; CMIP5 = Coupled Model Intercomparison Project Phase 5; CCSM = Community Climate System Model; CLM = community land model.

although MESM is still within the range of CMIP models. For total runoff, MESM produces more runoff on the global scale than the CMIP5 models (Table 3), although the predominant seasonal and latitudinal features are preserved (Figure 12). As previously discussed in section 2.4, the modification of the soil-infiltration scheme (i.e., removal of enhanced hydraulic conductivity under excessive dry soil conditions) was of considerable benefit to the performance of evapotanspiration and runoff rates shown here.

3.3.3. Ecosystem Productivity and Natural Emissions of Trace Gases

Net Ecosystem Productivity. The results from the key water and energy fluxes of the land system provide a first-order expectation to the climatological behavior of the terrestrial carbon cycle within MESM. As in previous evaluations of the land systems implemented within this Earth-system model framework (Schlosser et al., 2007), we focus on the net exchange of carbon between the land and the atmosphere, which represents a key coupling. Further, the TEM model is commonly used in a *stand-alone* configuration to simulate historical conditions and thus driven by observed atmospheric conditions (e.g., Zhu et al., 2011), and previous evaluations have used this as a baseline for TEM reduced-form configuration with the MESM framework (e.g., Schlosser et al., 2007). We extend this approach by considering the NEP of TEM on a month versus latitude projection (Figure 13). We find that the implementation of TEM within the MESM structure preserves all of the salient seasonal and latitudinal attributes as seen in previous evaluations (Figure 19 of Schlosser et al., 2007), and the characteristics of these patterns are consistent and corroborated by recent and detailed simulations with TEM in stand-alone configuration (e.g., Chen et al., 2011; Lu et al., 2015; Zhu & Zhuang, 2013). Overall, terrestrial ecosystems represented a net uptake of carbon both globally as well as across all latitudes through our historical period of evaluation (1981–2005). In addition, the strongest (annual) sinks of carbon that are found to be across the boreal latitude bands are composed of extensive forest cover. An additional smaller relative peak is also seen across the southern tropical latitudes. Although these areas are strong sinks —they carry a distinct seasonality and serve as considerable carbon sources during the late Fall through early Spring months.

Methane Emissions. In keeping with our overall approach to evaluate the performance of the land biogeochemical fluxes, we have evaluated the methane emissions against previous evaluations of models that

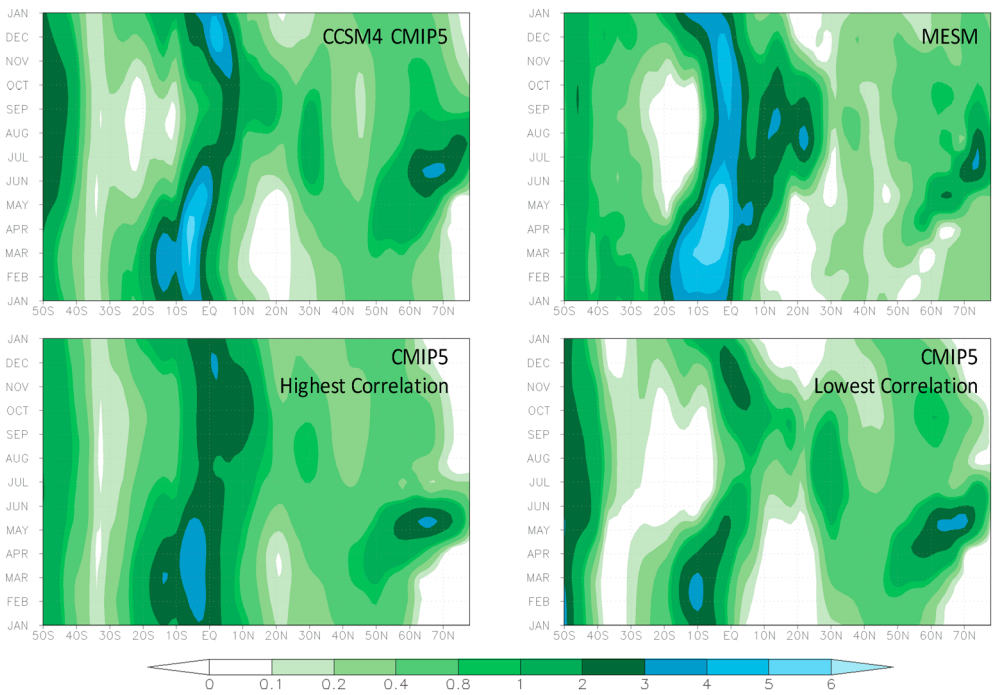

Figure 12. Month versus latitude profiles of runoff (mm/day) given by observations from the MESM (upper right panel), as well as two simulations from the CMIP5 (lower panels). The CMIP5 results show the two models with the highest (lower left) and lowest (lower right) pattern correlation with MESM. Also shown is the simulation from CCSM4 (upper left) panel. CCSM4 and the GLS component of MESM both use the CLM for the calculation of the land-surface water and energy budgets. MESM = MIT Earth System Model of intermediate complexity; MIT = Massachusetts Institute of Technology; CMIP5 = Coupled Model Intercomparison Project Phase 5; CCSM = Community Climate System Model; CLM = community land model; GLS = Global Land System.

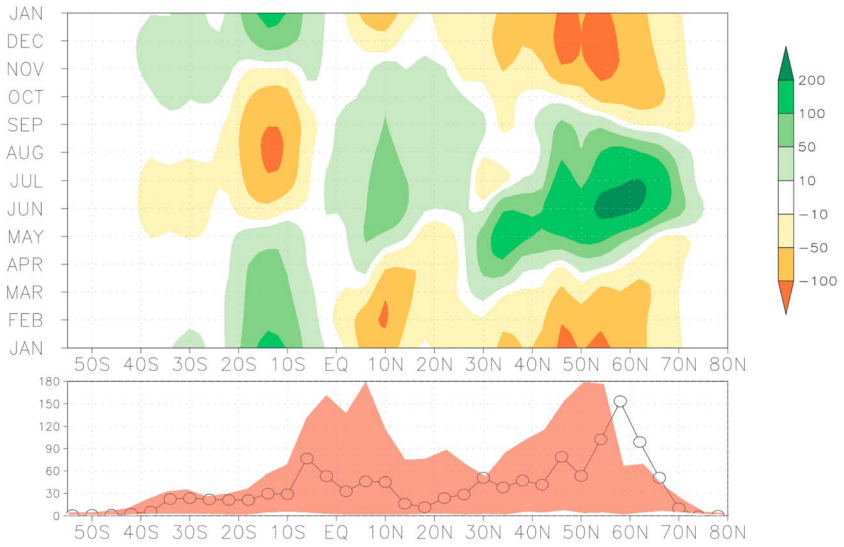

Figure 13. Simulations of net ecosystem productivity by the Massachusetts Institute of Technology Earth System Model within the Integrated Global System Model framework. Top panel displays the month versus latitude results averaged over 1981–2005, and the bottom panel shows the corresponding annual fluxes by latitude. Units are in 10^9 kg·C/month and 10^9 kg·C/year, respectively. Shown also in the bottom panel with the shaded red area is the multimodel range from five of the Coupled Model Intercomparison Project Phase 5 Earth system models that provided data from historical simulations that cover the evaluation period.

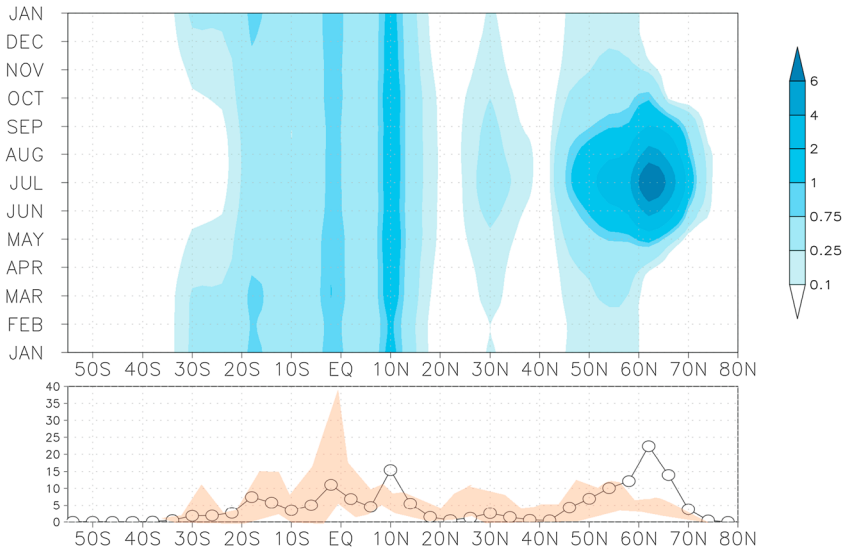

Figure 14. Simulations of emissions of methane by the MESM within the IGSM framework. Top panel displays the month versus latitude results (units in Tg·CH_4/month) averaged over 1993–2004, and the bottom panel shows the corresponding annual fluxes by latitude (units in Tg·CH_4/year). Shown also in the bottom panel with the shaded red area is the multimodel range from the results of WETCHIMP with. More recent studies (not shown in figure) indicate that the excess in emissions from MESM at high northern latitudes is credible (see corresponding text for details). MESM = MIT Earth System Model of intermediate complexity; MIT = Massachusetts Institute of Technology; IGSM = Integrated Global System Model.

contain similar core parameterization recipes but also a recent multimodel assessment (the WETCHIMP study of Melton et al., 2013) with distinct structural differences in overall design as well as implementation of the participating models. In order to provide the most consistent comparative evaluation in this regard, we focus on the historical period of 1993–2004. We find that for nearly all latitudes, the annual emission of methane from MESM falls within the range of the multimodel assessment (Figure 14). The most notable exception is found at boreal latitudes with the MESM estimate well above the upper bound of the WETCHIMP range. However, one notable feature of this multimodel assessment is that it did not contain a model participant with TEM as its core ecosystem model that MESM employs. Looking at model-based studies that have used TEM as the core ecosystem model (e.g., Zhuang et al., 2004) as well as an observation-based artificial neural network method (Zhu et al., 2013) to estimate total methane emissions in boreal latitudes (north of 45°N), they indicate values on the order of 44 to 54 Tg CH_4/year. The methane emission rates from the MESM historical simulation provide a more consistent latitude profile of emission across the boreal zone in this regard. Given that the higher boreal emission rates are more closely aligned to the observation-based result, we are confident that the MESM estimate is providing not only a result that is representative of the core ecosystem model behavior (i.e., TEM) but also a value that is empirically defensible.

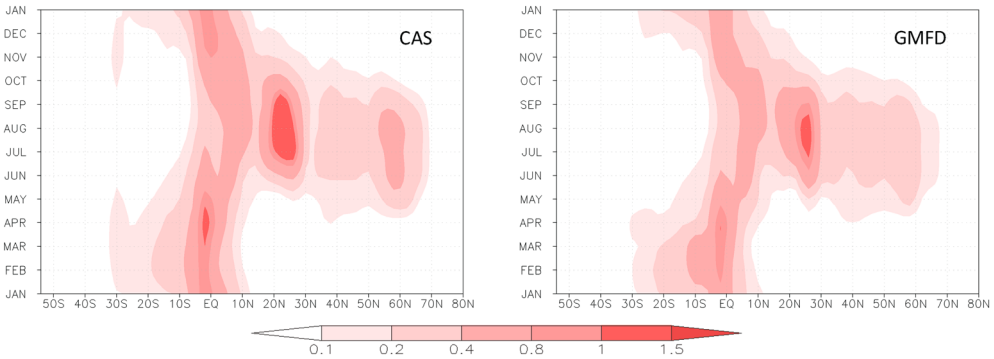

Figure 15. Simulations of soil emissions of nitrous oxide by the CLMCN-N_2O model (Saikawa et al., 2013) forced by two different meteorological data sets (CAS and GMFD). Shown are month versus latitude results averaged over 1981–2005. Units are in 10^8 kg·N_2O/month. CLMCN-N_2O = Community Land Model with Carbon and Nitrogen coupled to a N_2O emissions model.

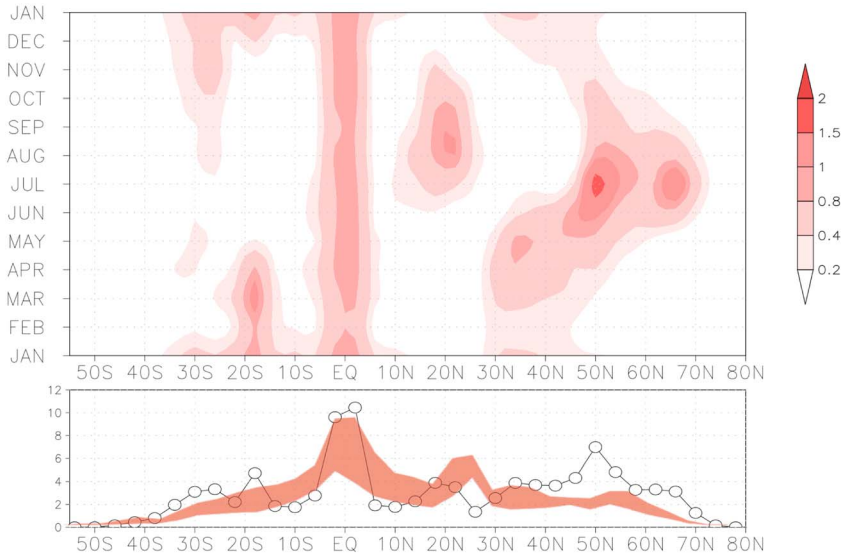

Figure 16. Simulations of soil emissions of nitrous oxide by the Massachusetts Institute of Technology Earth-System Model within the Integrated Global System Model framework. The top panel shows month versus latitude results averaged over 1981–2005 with units in 10^8 kg·N_2O/month. The bottom panel provides the annual emission rates (10^8 kg·N_2O/year) for the corresponding latitudes of the top panel. Shown also in the bottom panel with the shaded red area is a range based on the results from Saikawa et al. (2013) and Hashimoto (2012).

Nitrous Oxide. In a similar vein to our evaluation of NEP, we find that the MESM historical simulation and a standalone version of CLMCN coupled to a N_2O emissions model (CLMCN-N2O, Saikawa et al., 2013) share common features but also exhibit distinct differences. It is important, however, to note that this model-to-model comparison cannot provide any judgment on the fidelity or veracity of either model. Rather, this is an evaluation of the sensitivity to the configuration and application of the soil N_2O emissions module (a variant of the DNDC model) within and Earth system model framework. As such, both of the models exhibit consistent latitudinal locations of relative maximum emission rates (Figures 15 and 16)—which occur along the equator as well as during the summer season in both the northern and southern subtropical bands. Consistent across all these simulations is that the tropics provide the strongest annual emission source. While both models provide an additional source of emissions across the mid and higher northern latitude bands, a distinct difference is seen in the seasonality of this feature. The CLMCN-N2O model exhibits a distinct summertime peak in emissions that is coincident and widespread across the middle and into higher latitudes. In the MESM zonal configuration—the extent and summer timing of the peak is aligned with the CLMCN-N2O estimate between 45° and 75°N; however, for latitudes 25°–45°N there is an earlier onset and terminus of this feature. Through the course of a number of variants and sensitivity simulations with the IGSM, we have identified that the most likely culprit to this behavior lies within the MESM simulation of land precipitation. When compared to an observationally based estimate (GPCP), we find that the MESM estimate of precipitation is biased low during the summertime across the corresponding latitude bands (Figure 10). In conjunction with low evapotranspiration rates during the spring (not shown)—soil moisture stores become elevated at these latitudes and trigger the soil anaerobic conditions necessary for denitrification, and thus leads to the earlier emissions peak. However, by the beginning of the summer—elevated evapotranspiration levels combined with a precipitation deficit support dry soils and the emissions processes in MESM become dormant. Nevertheless, we have made salient progress from our earlier implementation (Schlosser et al., 2007) in providing a more consistent depiction of soil N_2O emissions with a reduced form of

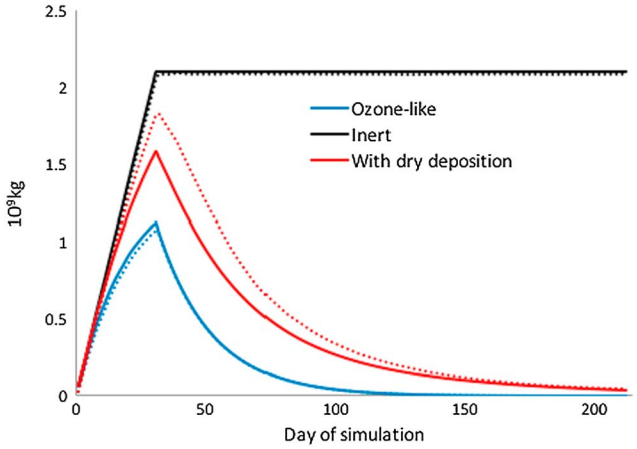

Figure 17. Time evolutions of total mass (10^9 kg) for inert ozone-like and tracer with dry deposition in simulations with January emissions with Massachusetts Institute of Technology Earth-System Model (solid lines) and GEOS-Chem (dashed lines). GEOS= Goddard Earth Observing System.

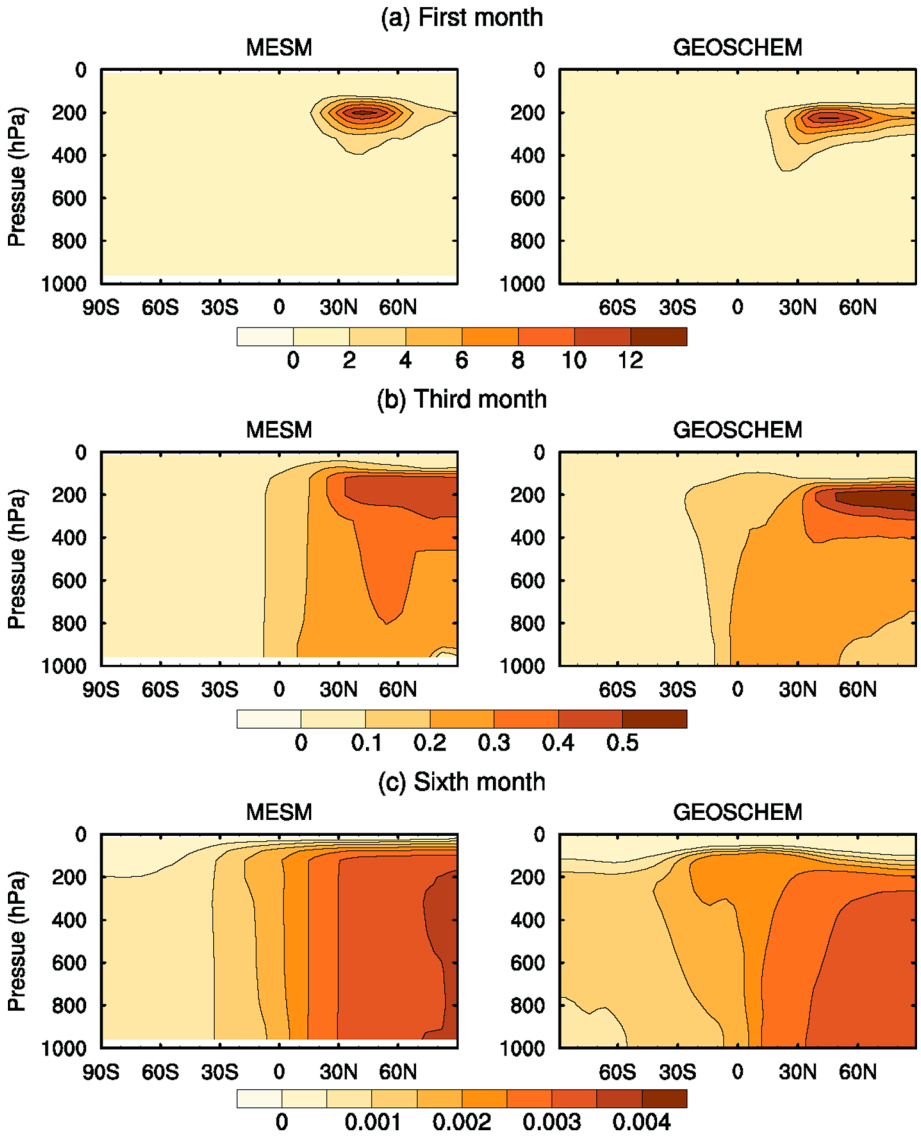

Figure 18. Latitude-pressure distributions of ozone-like tracer concentration (ppbm) in simulations with January emissions for first (top), third (middle), and sixth (bottom) months of simulation. (left column) Results obtained with the MIT MESM. (right column) Result from GEOS-Chem. GEOS= Goddard Earth Observing System.

the model compared to its more detailed counterpart. The scientific community has recently recognized key areas for improvement (Butterbach-Bahl et al., 2013) and will continue to make necessary strides in the detailed modeling of nitrous oxide emissions and verification studies. As such, this strategy will continue to be a critical element of our model development, particularly with regard to the N_2O emissions component.

3.4. Emissions-Driven Projections of Future Climate

In the simulations discussed below, the MESM was forced by anthropogenic emissions calculated by the EPPA model, including carbon emissions associated with land use. MESM also takes into account natural emissions of CH_4 and N_2O calculated by NEM.

Wang et al. (1998) describe a tropospheric chemistry and transport scheme for a chemical tracer used in the MESM. Tracer transport by eddies, which cannot be explicitly simulated by zonal atmospheric model, is parameterized similar to moisture transport. In the framework of the Aviation Climate Change Research Initiative (ACCRI, Brasseur et al., 2016), the MESM was used in a tracer transport comparison exercise. In these simulations, the ACCRI 2006 fuel burn inventory (Barrett et al., 2010) above 8 km were used as a proxy for tracer emissions. Simulations were carried out for 6 months starting in January and July with tracers being

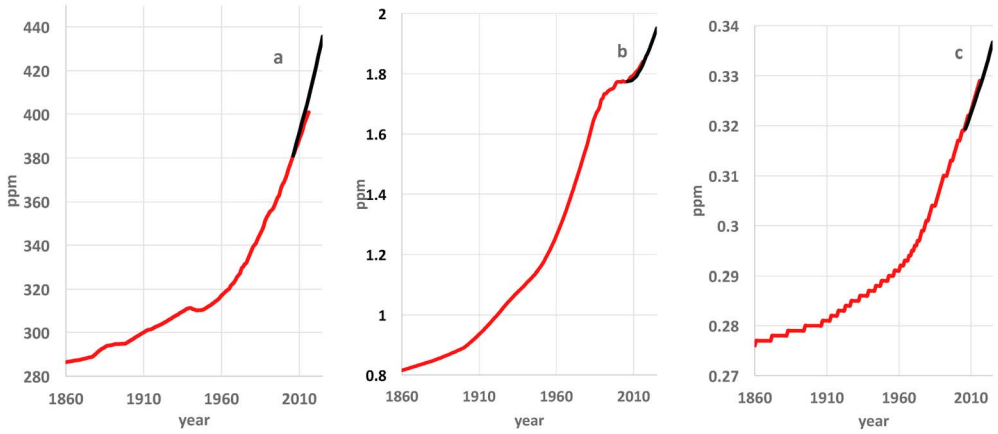

Figure 19. Observed (red) and projected (black) concentrations of CO_2 (left), CH_4 (middle), and N_2O (right).

released in the atmosphere during the first month only. Below we show comparisons between results obtained in simulations with the MESM and GEOS-Chem models for three different types of tracers: an inert tracer (no losses), a tropospheric ozone-like tracer with a prescribed 21-day *e*-folding lifetime, and a tracer with a dry deposition removal process. Results are shown only for simulations that started in January, because results of simulations that started in July look very similar. The total mass of the tracer with dry deposition decreases slightly faster in simulations with MESM than with GEOS-Chem, while the changes for the other two tracers are practically identical in both model simulations (Figure 17). Figure 18 shows latitude- pressure distributions for the ozone-like tracer for the first, third, and sixth months of the simulations. Because the total mass of the tracer decreases exponentially, data for the third and sixth months were multiplied by factors of 10 and 10^4, respectively. In general, the study of the impact of aviation emissions on atmospheric chemical composition and climate showed that MESM results lie well within the envelope of the more complex 3-D chemistry-climate models (Olsen et al., 2013).

Our simulations with interactive chemistry start in year 2006 as a continuation of a historical simulation, and future projections are then usually given to 2100. Here, however, we will concentrate on short-term simulations (2006–2015) when model mixing ratios using model emissions can be compared with observed mixing ratios.

As can be seen, the MESM simulates global concentrations of the three major long-lived greenhouse gases rather well (Figure 19). Figure 20 plots tropospheric mixing ratios for some climate-relevant species (O_3, CH_4, CO, SO_2, NO, and NO_2) as well as the very short-lived OH species from the MESM output and the zonal average for the Atmospheric Chemistry and Climate Model Intercomparison Project (ACCMIP) archived version of the CESM CAM-Chem, with CAM version 3.5 (available at http://browse.ceda.ac.uk/browse/badc/accmip). The CESM output has 26 vertical levels, which have been regridded to match the 11-level MESM output in Figure 20. In general, the MESM results are comparable to the CESM data, with the vertical and latitudinal distributions of O_3, CH_4, and OH in fairly close agreement. The MESM does not have the hemispheric asymmetries for CO and NO_2 that are shown in the CESM data, and the MESM vertical distribution of SO_2 peaks at the third level, as a result of SO_2 emissions being distributed evenly in the bottom two layers. In addition, in contrast to most chemistry models (including the CESM-CAM-Chem), MESM does not use prescribed surface concentrations as low boundary conditions.

The radiative forcing and the simulated surface air temperature (not shown) are almost identical in historical (concentration-driven) and emissions-driven simulations. In general, the simulated climates are very similar during the overlapping period of the two simulations (2006–2010).

4. Conclusions

This paper describes the current version of the MIT Earth System Model. The MESM belongs to the class of Earth system models of intermediate complexity, which occupy a place between simple conceptual models and comprehensive global circulation models (Claussen et al., 2002). It provides a physical representation of key climate processes and feedbacks, while remaining computationally efficient, and thus allowing for large

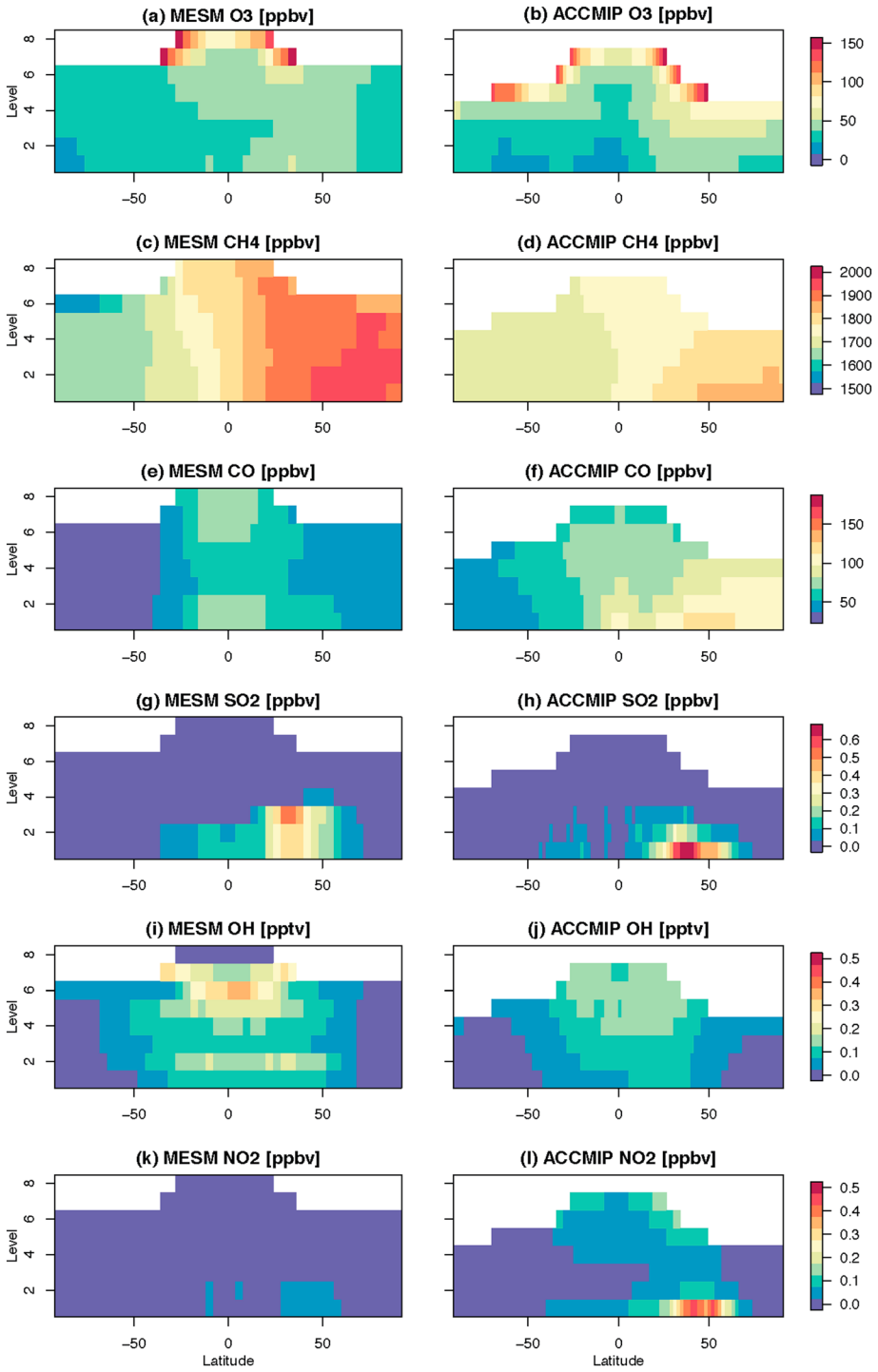

Figure 20. Present-day simulated zonal output from the MESM (left) and zonally averaged output from the CESM CAM-Chem, CAM version 3.5 archived data from the ACCMIP archive (right) for O_3, CH_4, CO, SO_2, OH, and NO_2. The CAM data have been regridded to match the MESM levels, and only data below the tropopause (here defined as 150 ppbv O3) is shown. MESM = MIT Earth System Model of intermediate complexity; MIT = Massachusetts Institute of Technology. CESM CAM = Community Earth System Model, Community Atmosphere Model; ACCMIP = Atmospheric Chemistry and Climate Model Intercomparison Project.

ensemble of climate simulations to be conducted at significantly less cost than state-of-the-art climate models. The number of climate system components and their complexity are defined by the nature of studies for which the model is intended to be used in. The MESM is designed for and has been used in two major types of studies. First, the MESM has been used to evaluate the uncertainty in key parameters controlling the climate system response to changes in external forcing. Large ensembles of climate simulations are run under historical concentrations of greenhouse gases and aerosols, while the relevant climate model parameters are systematically varied (e.g., climate sensitivity, rate of ocean heat uptake, and strength of the net aerosol forcing). The simulated climate is then compared with available observations using optimal fingerprint diagnostics to derive probability distributions of the parameters (Forest et al., 2002, 2008; Libardoni & Forest, 2011, 2013). Second, the MESM has been used to investigate the uncertainty in future climate projections arising from the uncertainty in the climate system response to changes in external forcing and the uncertainty in future human activity. This is done by running large ensemble of climate simulations with Latin hypercube sampling of the key climate parameters from their probability distributions under various greenhouse gas and aerosols emissions scenarios developed with the EPPA model (Sokolov et al., 2009; Webster et al., 2012).

Key model requirements to conduct such analysis are as follows: (i) the capability to vary key climate model parameters over a wide range representative of our current knowledge of the climate system, (ii) computational efficiency in order to run large ensemble for robust uncertainty quantification, and (iii) the availability of a comprehensive chemistry model to simulate the fate of various radiatively active chemical species and their impact on the climate system. Since our studies showed that the rate of heat uptake in a three-dimensional dynamical ocean general circulation model can only be changed over a rather narrow range (Dutkiewicz et al., 2005; Sokolov et al., 2007), the version of MESM used in uncertainty studies incorporates a simplified ADOM, in which the ocean heat uptake rate can be varied over a much wider range. Computational efficiency, required to perform thousands of simulations, is achieved by using a zonally averaged atmospheric model. Nonetheless, the MESM includes a rather comprehensive chemistry model, which can simulate the interaction between different chemical species, such as an impact of changes in NO_x emissions on methane lifetime, and the interaction between climate and chemistry, such as an impact of changes in surface ozone concentration on productivity of terrestrial ecosystem (Felzer et al., 2004, 2005). As a result, the MESM can be used to evaluate the uncertainty in future climate projections associated with different emission scenarios, accounting for complex interactions and feedbacks between atmospheric chemistry, carbon cycle, and climate.

While not originally designed for such purposes, the MESM has also been used for multicentennial climate simulations, such as projections beyond 2300 to investigate longer-term commitment and irreversibility (Zickfeld et al., 2013) or preindustrial portions of the last millennium to assess historical carbon-climate feedbacks (Eby et al., 2013).

The MESM is primarily used to simulate changes in global mean climate variables. In spite of deficiencies in simulated zonal distributions of different climate variables for present-day climate, it reasonably well simulates zonal structure of climate change. In addition, the MESM has been combined with statistical climate emulator techniques, such as pattern scaling (Monier et al., 2015; Schlosser et al., 2013), to compute regional climate information that accounts not only for the uncertainty in the global climate system response and human activity but also for the uncertainty in the regional patterns of climate change associated with different climate models. For example, the MESM has been used to derive probabilistic distributions of changes in temperature and precipitation over Northern Eurasia (Monier et al., 2013). Large ensembles of regional climate simulations using the MESM were also used to investigate the risk of permafrost degradation and the associated high-latitude methane emissions (Gao et al., 2013), to compute probabilistic projections of water stress over a large portion of Asia (Fant et al., 2016), and to examine the climate change and economic growth prospects for agriculture, road infrastructure, and hydropower generation in Malawi (Arndt et al., 2014).

Overall, the results presented in the paper show that, despite simplifications made in the model, the MESM simulates rather well changes in observed climate since the middle of the 19th century as well as the main features of present-day climate. The results of the simulations performed in emissions-driven model also compare favorably with results obtained with comprehensive climate-chemistry models and available observations. Therefore, the MESM provide a valuable and efficient tool for climate change modeling, uncertainty quantification, and climate risk analysis.

Acknowledgments
We thank two anonymous reviewers for useful comments that help to improve the paper. This work was supported by U.S. Department of Energy (DOE), Office of Science under DE-FG02-94ER61937 and other government, industry, and foundation sponsors of the MIT Joint Program on the Science and Policy of Global Change. For a complete list of sponsors and U.S. government funding sources, see http://globalchange.mit.edu/sponsors/. Data presented in the paper are available at http://hdl.handle.net/1721.1/113339

References

Adler, R. F., Gu, G., & Huffman, G. (2012). Estimating climatological bias errors for the Global Precipitation Climatology Project (GPCP). *Journal of Applied Meteorology and Climatology*, *51*(1), 84–99. https://doi.org/10.1175/JAMC-D-11-052.1

Adler, R. F., Huffman, G. J., Chang, A., Ferraro, R., Xie, P., Janowiak, J., et al. (2003). The version 2 Global Precipitation Climatology Project (GPCP) monthly precipitation analysis (1979–present). *Journal of Hydrometeorology*, *4*(6), 1147–1167. https://doi.org/10.1175/1525-7541(2003)004<1147:TVGPCP>2.0.CO;2

Andrews, T., Gregory, J. M., Webb, M. J., & Taylor, K. E. (2012). Forcing, feedbacks and climate sensitivity in CMIP5 coupled atmosphere-ocean climate models. *Geophysical Research Letters*, *39*, L09712. https://doi.org/10.1029/2012GL051607

Andronova, N. G., & Schlesinger, M. E. (2001). Objective estimation of the probability density function for climate sensitivity. *Journal of Geophysical Research*, *106*, 22,605–22,611. https://doi.org/10.1029/2000JD000259

Arndt, C., Schlosser, A., Strzepek, K., & Thurlow, J. (2014). Climate change and economic growth prospects for Malawi: An uncertainty approach. *Journal of African Economies*, *23*(suppl 2), ii83–ii107. https://doi.org/10.1093/jae/eju013

Barrett, S., Prather, M., Penner, J., Selkirk, H., Balasubramanian, S., Dopelheuer, A., et al. (2010). Guidance on the use of AEDT gridded aircraft emissions in atmospheric models. MIT The Laboratory for Aviation and the Environment (Rep. LAE-2010-008-N, 13 pp.). Retrieved from http://lae.mit.edu/uploads/LAE_report_series/2010/LAE-2010-008-N.pdf

Bonan, G. B., Oleson, K. W., Vertenstein, M., Lewis, S., Zeng, X., Dai, Y., et al. (2002). The land surface climatology of the community land model coupled to the NCAR community climate model. *Journal of Climate*, *15*(22), 3123–3149. https://doi.org/10.1175/1520-0442(2002)015<3123:TLSCOT>2.0.CO;2

Bony, S., Colman, R., Kattsov, V. M., Allan, R. P., Bretherton, C. S., Dufresne, J. L., et al. (2006). How well do we understand and evaluate climate change feedback processes. *Journal of Climate*, *19*(15), 3445–3482. https://doi.org/10.1175/JCLI3819.1

Brasseur, G., Gupta, M., Anderson, B. E., Balasubramanian, S., Barrett, S., Duda, D., et al. (2016). Impact of aviation on climate: FAA's Aviation Climate Change Research Initiative (ACCRI) Phase II. *Bulletin of the American Meteorological Society*, *97*(4), 561–583. https://doi.org/10.1175/BAMS-D-13-00089.1

Brovkin, V., Claussen, M., Driesschaert, E., Fichefet, T., Kicklighter, D., Loutre, M. F., et al. (2006). Biogeophysical effects of historical land cover changes simulated by six Earth system models of intermediate complexity. *Climate Dynamics*, *26*(6), 587–600. https://doi.org/10.1007/s00382-005-0092-6

Butterbach-Bahl, K., Baggs, E. M., Dannenmann, M., Kiese, R., & Zechmeister- Boltenstern, S. (2013). Nitrous oxide emissions from soils: How well do we understand the processes and their controls? *Philosophical Transactions of the Royal Society B*, *368*(1621). https://doi.org/10.1098/rstb.2013.0122

Calbó, J., Pan, W., Webster, M., Prinn, R. G., & McRae, G. J. (1998). Parameterization of urban sub-grid scale processes in global atmospheric chemistry models. *Journal of Geophysical Research*, *103*, 3437–3451. https://doi.org/10.1029/97JD02654

Cess, R. D., Potter, G. L., Blanchet, J. P., Boer, G. J., Del Genio, A. D., Lacis, A. A., et al. (1990). Intercomparison and Interpretation of climate feedback processes in 19 atmospheric general circulation models. *Journal of Geophysical Research*, *95*, 16,601–16,615.

Chen, M., Zhuang, Q., Cook, D. R., Coulter, R., Pekour, M., Scott, R. L., et al. (2011). Quantification of terrestrial ecosystem carbon dynamics in the conterminous United States combining a process-based biogeochemical model and MODIS and AmeriFlux data. *Biogeosciences*, *8*(9), 2665–2688. https://doi.org/10.5194/bg-8-2665-2011

Chen, Y.-H., Paltsev, S., Reilly, J., Morris, J., & Babiker, M. (2016). Long-term economic modeling for climate change assessment. *Economic Modeling*, *52*, 867–883. https://doi.org/10.1016/j.econmod.2015.10.023

Cionni, I., Eyring, V., Lamarque, J. F., Randel, W. J., Stevenson, D. S., Wu, F., et al. (2011). Ozone database in support of CMIP5 simulations: Results and corresponding radiative forcing. *Atmospheric Chemistry and Physics*, *11*, 11, 267–11, 292.

Claussen, M., Mysak, L. A., Weaver, A. J., Crucifix, M., Fichefet, T., Loutre, M.-F., et al. (2002). Earth system models of intermediate complexity: Closing the gap in the spectrum of climate system models. *Climate Dynamics*, *15*, 579–586.

Colman, R. (2003). A comparison of climate feedbacks in general circulation models. *Climate Dynamics*, *20*(7-8), 865–873. https://doi.org/10.1007/s00382-003-0310-z

Cowtan, K., Hausfather, Z., Hawkins, E., Jacobs, P., Mann, M. E., Miller, S. K., et al. (2015). Robust comparison of climate models with observations using blended land air and ocean sea surface temperatures. *Geophysical Research Letters*, *42*, 6526–6534. https://doi.org/10.1002/2015GL064888

Cramer, W. P., & Leemans, R. (2001). Global 30-year mean monthly climatology, 1930–1960, National Laboratory Distributed Active Archive Center, Oak Ridge, Tennessee, U.S.A. Data set. Retrieved from http://www.daac.ornl.gov

Curtis, P. S., & Wang, X. (1998). A meta-analysis of elevated CO_2 effects on woody plant mass, form, and physiology. *Oecologia*, *113*(3), 299–313. https://doi.org/10.1007/s004420050381

Dutkiewicz, S., Sokolov, A., Scott, J., & Stone, P. (2005). A three-dimensional ocean-seaice-carbon cycle model and its coupling to a two-dimensional atmospheric model: Uses in climate change studies. Report 122, MIT Joint Program on the Science and Policy of Global Change (http://mit.edu/globalchange/www/MITJPSPGC_Rpt122.pdf).

Eby, M., Weaver, A. J., Alexander, K., Zickfeld, K., Abe-Ouchi, A., Cimatoribus, A. A., et al. (2013). Historical and idealized climate model experiments: An intercomparison of Earth system models of intermediate complexity. *Climate Pastoralism*, *9*, 1111–1140.

Fant, C., Schlosser, C. A., Gao, X., Strzepek, K., & Reilly, J. (2016). Projections of water stress based on an ensemble of socioeconomic growth and climate change scenarios: A case study in Asia. *PLoS One*, *11*(3), e0150633. https://doi.org/10.1371/journal.pone.0150633

Felzer, B., Kicklighter, D., Melillo, J., Wang, C., Zhuang, Q., & Prinn, R. (2004). Effects of ozone on net primary production and carbon sequestration in the conterminous United States using a biogeochemistry model. *Tellus B*, *56*(3), 230–248. https://doi.org/10.1111/j.1600-0889.2004.00097.x

Felzer, B., Reilly, J., Melillo, J., Kicklighter, D., Sarofim, M., Wang, C., et al. (2005). Future effects of ozone on carbon sequestration and climate change policy using a global biogeochemical model. *Climatic Change*, *73*(3), 345–373. https://doi.org/10.1007/s10584-005-6776-4

Forest, C. E., Stone, P. H., & Sokolov, A. P. (2008). Constraining climate model parameters from observed 20th century changes. *Tellus*, *60A*, 911–920.

Forest, C. E., Stone, P. H., Sokolov, A. P., Allen, M. R., & Webster, M. (2002). Quantifying uncertainties in climate system properties with the use of recent climate observations. *Science*, *295*(5552), 113–117. https://doi.org/10.1126/science.1064419

Forster, P. M., Andrews, T., Good, P., Gregory, J. M., Jackson, L. S., & Zelinka, M. (2013). Evaluating adjusted forcing and model spread for historical and future scenarios in the CMIP5 generation of climate models. *Journal of Geophysical Research: Atmospheres*, *118*, 1139–1150. https://doi.org/10.1002/jgrd.50174

Friedlingstein, P., Cox, P., Betts, R., Bopp, L., von Bloh, W., Brovkin, V., et al. (2006). Climate–carbon cycle feedback analysis: Results from the C^4MIP model Intercomparison. *Journal of Climate*, *19*(14), 3337–3353. https://doi.org/10.1175/JCLI3800.1

Friedlingstein, P., Meinshausen, M., Arora, V. K., Jones, C. D., Anav, A., Liddicoat, S. K., & Knutti, R. (2014). Uncertainties in CMIP5 climate projections due to carbon cycle feedbacks. *Journal of Climate*, *27*(2), 511–526. https://doi.org/10.1175/JCLI-D-12-00579.1

Galford, G. L., Melillo, J. M., Kicklighter, D. W., Cronin, T. W., Cerri, C. E. P., Mustard, J. F., & Cerri, C. C. (2010). Greenhouse gas emissions from alternative futures of deforestation and agricultural management in the southern Amazon. *Proceedings of the National Academy of Sciences*, *107*(46), 19,649–19,654. https://doi.org/10.1073/pnas.1000780107

Galford, G. L., Melillo, J. M., Kicklighter, D. W., Mustard, J. F., Cronin, T. W., Cerri, C. E. P., & Cerri, C. C. (2011). Historical carbon emissions and uptake from the agricultural frontier of the Brazilian Amazon. *Ecological Applications*, *21*(3), 750–763. https://doi.org/10.1890/09-1957.1

Gao, X., Schlosser, C. A., Sokolov, A. P., Anthony, K. W., Zhuang, Q., & Kicklighter, D. (2013). Permafrost degradation and methane: Low risk of biogeochemical climate-warming feedback. *Environmental Research Letters*, *8*(3), 035014. https://doi.org/10.1088/1748-9326/8/3/035014

Gelaro, R., McCarty, W., Suáreza, M. J., Todling, R., Molod, A., Takacs, L., et al. (2017). The modern-era retrospective analysis for research and applications, version 2 (MERRA-2). *Journal of Climate*, *30*, 5419–5454. https://doi.org/10.1175/JCLI-D-16-0758.1

Gillet, N. P., Arora, V. K., Matthews, D., & Allen, M. R. (2013). Constraining the ratio of global warming to cumulative CO_2 emissions using CMIP5 simulations. *Journal of Climate*, *26*, 6844–6858.

Gregory, J. M., Dixon, K. W., Stouffer, R. J., Weaver, A. J., Driesschaert, E., Eby, E., et al. (2005). A model intercomparison of changes in the Atlantic thermohaline circulation in response to increasing atmospheric CO_2 concentration. *Geophysical Research Letters*, *32*, L12703. https://doi.org/10.1029/2005GL023209

Gregory, J. M., Stouffer, R. J., Raper, S. C. B., Stott, P. A., & Rayner, N. A. (2002). An observationally based estimate of the climate sensitivity. *Journal of Climate*, *15*(22), 3117–3121. https://doi.org/10.1175/1520-0442(2002)015<3117:AOBEOT>2.0.CO;2

Gunderson, C. A., & Wullschleger, S. D. (1994). Photosynthetic acclimation in trees to rising atmospheric CO_2: A broader perspective. *Photosynthesis Research*, *39*(3), 369–388. https://doi.org/10.1007/BF00014592

Hansen, J., Fung, I., Lacis, A., Rind, D., Lebedeff, S., Ruedy, R., & Russell, G. (1988). Global climate change as forecast by Goddard Institute for space studies three-dimensional model. *Journal of Geophysical Research*, *93*, 9341–9364. https://doi.org/10.1029/JD093iD08p09341

Hansen, J., Lacis, A., Rind, D., Russell, G., Stone, P., Fung, I., et al. (1984). Climate sensitivity: Analysis of feedback mechanisms. In J. E. Hansen & T. Takahashi (Eds.), *Climate processes and climate sensitivity, geophysical monograph* (pp. 130–163). Washington, DC: American Geophysical Union. https://doi.org/10.1029/GM029p0130

Hansen, J., Lacis, A., Ruedy, R., Sato, M., & Wilson, H. (1993). How sensitive is world's climate. *National Geographic Research and Exploration*, *9*, 142–158.

Hansen, J., Russell, G., Rind, D., Stone, P., Lacis, A., Lebedeff, S., et al. (1983). Efficient three-dimensional global models for climate studies: Models I and II. *Monthly Weather Review*, *111*(4), 609–662. https://doi.org/10.1175/1520-0493(1983)111<0609:ETDGMF>2.0.CO;2

Hansen, J., Sato, M., Ruedy, R., Kharecha, P., Lacis, A., Miller, R., et al. (2007). Climate simulations for 1880–2003 with GISS model E. *Climate Dynamics*, *29*. https://doi.org/10.1007/s00382–007–0255–8

Hashimoto, S. (2012). A New Estimation of Global Soil Greenhouse Gas Fluxes Using a Simple Data-Oriented Model. *PLoS One*, *7*(11). https://doi.org/10.1371/annotation/4526d447-db8e-4bb7-831c-752b8498a63d

Holian, G.L., Sokolov, A.P., & Prinn, R. G. (2001), Uncertainty in atmospheric CO_2 predictions from a global ocean carbon cycle model. Report 80, MIT Joint Program on the Science and Policy of Global Change (Report 80, 25 pp.). Retrieved from http://web.mit.edu/globalchange/www/MITJPSPGC_Rpt80.pdf

Intergovernmental Panel on Climate Change (IPCC) (2013). Summary for Policymakers. In T. F. Stocker, et al. (Eds.), *Climate change 2013: The physical science basis, contribution of Working Group I to the Fifth Assessment Report of the Intergovernmental Panel on Climate Change* (pp. 3–29). Cambridge: Cambridge University Press.

Jones C., Robertson, E., Arora, V., Friedlingstein, P., Shevliakova, E., Bopp, L., et al. (2013). Twenty-first-century compatible CO_2 emissions and airborne fraction simulated by CMIP5 Earth System Models under four Representative Concentration Pathways. *Journal of Climate*, *26*, 4398–4413. https://doi.org/10.1175/JCLI-D-12-00554.1

Kamenkovich, I. V., Sokolov, A., & Stone, P. H. (2002). An efficient climate model with a 3D ocean and statistical-dynamical atmosphere. *Climate Dynamics*, *19*(7), 585–598.

Kicklighter, D. W., Cai, Y., Zhuang, Q., Parfenova, E. I., Paltsev, S., Sokolov, A. P., et al. (2014). Potential influence of climate-induced vegetation shifts on future land use and associated land carbon fluxes in northern Eurasia. *Environmental Research Letters*, *9*(3), 035004. https://doi.org/10.1088/1748-9326/9/3/035004

Kicklighter, D. W., Gurgel, A. C., Melillo, J. M., Reilly, J. M., & Paltsev, S. (2012) Potential direct and indirect effects of global cellulosic biofuel production on greenhouse gas fluxes from future land-use change. MIT joint program on science and policy of global change report no. 210. Massachusetts Institute of Technology, Cambridge, MA. Retrieved from https://globalchange.mit.edu/publication/14325

Klimont, Z., Smith, S. J., & Cofala, J. (2013). The last decade of global anthropogenic sulfur dioxide: 2000–2011 emissions. *Environmental Research Letters*, *8*(1). https://doi.org/10.1088/1748–9326/8/1/014003

Knutti, R., Stoker, T. F., Joos, F., & Plattner, G.-K. (2003). Probabilistic climate change projections using neural network. *Climate Dynamics*, *21*(3-4), 257–272. https://doi.org/10.1007/s00382-003-0345-1

Kopp, G., & Lean, J. L. (2011). A new, lower value of total solar irradiance: Evidence and climate significance. *Geophysical Research Letters*, *38*, L01706. https://doi.org/10.1029/2010GL045777

Lawrence, D. M., Oleson, K. W., Flanner, M. G., Thornton, P. E., Swenson, S. C., Lawrence, P. J., et al. (2011). Parameterization improvements and functional and structural advances in version 4 of the community land model. *Journal of Advances in Modeling Earth Systems*, *3*(3). https://doi.org/10.1029/2011MS000045

Le Quere, C., Andrew, R. M., Canadell, J. G., Sitch, S., Korsbakken, J. I., Peters, G. P., et al. (2016). Global carbon budget 2016. *Earth System Science Data*, *8*, 605–649. https://doi.org/10.5194/essd-8-605-2016

Le Quéré, C., Andrew, R. M., Friedlingstein, P., Sitch, S., Pongratz, J., Manning, A. C., et al. (2018). Global carbon budget 2017. *Earth System Science Data Discussions*, *10*, 405–448.

Levitus, S., Antonov, J. T., Boyer, T. P., Baranova, O. K., Garcia, H. E., Locarnini, R. A., et al. (2012). World ocean heat content and thermosteric sea level change (0–2000 m), 1955–2010. *Geophysical Research Letters*, *39*, L10603. https://doi.org/10.1029/2012GL051106

Libardoni, A. (2017). Improving constraints on climate system properties with additional data and new methods, A dissertation in meteorology. The Pennsylvania State University, The Graduate School, College of Earth and Mineral Science.

Libardoni, A. G., & Forest, C. E. (2011). Sensitivity of distributions of climate system properties to the surface temperature dataset. *Geophysical Research Letters*, *38*, L22705. https://doi.org/10.1029/2011GL049431

Libardoni, A. G., & Forest, C. E. (2013). Correction to "sensitivity of distributions of climate system properties to the surface temperature data set". *Geophysical Research Letters*, *40*, 2309–2311. https://doi.org/10.1002/grl.50480

Liu, Y. (1996). Modeling the emissions of nitrous oxide (N_2O) and methane (CH_4) from the terrestrial biosphere to the atmosphere (PhD thesis), MIT. Joint program on the science and policy of global change (Report 10, 219 pp.). Cambridge, MA.

Lu, X., Kicklighter, D. W., Melillo, J. M., Reilly, J. M., & Xu, L. (2015). Land carbon sequestration within the conterminous United States: Regional- and state-level analyses. *Journal of Geophysical Research: Biogeosciences*, *120*, 379–398. https://doi.org/10.1002/2014JG002818

Matthews, H. D., Gillett, N. P., Stott, P. A., & Zickfeld, K. (2009). The proportionality of global warming to cumulative carbon emissions. *Nature*, *2*(459), 829–832. https://doi.org/10.1038/nature08047

Mayer, M., Wang, C., Webster, M., & Prinn, R. G. (2000). Linking local air pollution to global chemistry and climate. *Journal of Geophysical Research*, *105*, 22,869–22,896. https://doi.org/10.1029/2000JD900307

McGuire, A. D., Melillo, J. M., & Joyce, L. A. (1995). The role of nitrogen in the response of forest net primary production to elevated atmospheric carbon dioxide. *Annual Review of Ecology and Systematics*, *26*(1), 473–503. https://doi.org/10.1146/annurev.es.26.110195.002353

McGuire, A. D., Melillo, J. M., Joyce, L. A., Kicklighter, D. W., Grace, A. L., Moore, B. III, & Vorosmarty, C. J. (1992). Interactions between carbon and nitrogen dynamics in estimating net primary productivity for potential vegetation in North America. *Global Biogeochemical Cycles*, *6*, 101–124. https://doi.org/10.1029/92GB00219

McGuire, A. D., Melillo, J. M., Kicklighter, D. W., Pan, Y., Xiao, X., Helfrich, J., et al. (1997). Equilibrium responses of global net primary production and carbon storage to doubled atmospheric carbon dioxide: Sensitivity to changes in vegetation nitrogen concentration. *Global Biogeochemical Cycles*, *11*, 173–189. https://doi.org/10.1029/97GB00059

Meinshausen, M., Raper, S., & Wigley, T. (2011). Emulating coupled atmosphere-ocean and carbon cycle models with a simpler model, MAGICC6–Part 1: Model description and calibration. *Atmospheric Chemistry and Physics*, *11*(4), 1417–1456. https://doi.org/10.5194/acp-11-1417-2011

Melillo, J. M., Lu, X., Kicklighter, D. W., Reilly, J. M., Cai, Y., & Sokolov, A. P. (2016). Protected areas' role in climate-change mitigation. *Ambio*, *45*(2), 133–145. https://doi.org/10.1007/s13280-015-0693-1

Melillo, J. M., McGuire, A. D., Kicklighter, D. W., Moore, B. III, Vorosmarty, C. J., & Schloss, A. L. (1993). Global climate change and terrestrial net primary production. *Nature*, *363*(6426), 234–240. https://doi.org/10.1038/363234a0

Melillo, J. M., Reilly, J. M., Kicklighter, D. W., Gurgel, A. C., Cronin, T. W., Paltsev, S., et al. (2009). Indirect emissions from biofuels: How important? *Science*, *326*(5958), 1397–1399. https://doi.org/10.1126/science.1180251

Melton, J. R., Wania, R., Hodson, E. L., Poulter, B., Ringeval, B., Spahni, R., et al. (2013). Present state of global wetland extent and wetland methane modelling: Conclusions from a model inter-comparison project (WETCHIMP). *Biogeosciences*, *10*(2), 753–788. https://doi.org/10.5194/bg-10-753-2013

Millar, R. J., Otto, A., Forster, P. M., Lowe, J. A., Ingram, W. J., & Allen, M. R. (2015). Model structure in observational constraints on transient climate response. *Climatic Change*, *131*(2), 199–211. https://doi.org/10.1007/s10584-015-1384-4

Miller, R. L., G.A. Schmidt, L.S. Nazarenko, N. Tausnev, S.E. Bauer, A.D. Del Genio¸ et al., 2014: CMIP5 historical simulations (1850–2012) with GISS model E2. *Journal of Advances in Modeling Earth Systems, 6*, 441–478, 2. https://doi.org/10.1002/2013MS000266.

Monier, E., Gao, X., Scott, J. R., Sokolov, A. P., & Schlosser, C. A. (2015). A framework for modeling uncertainty in regional climate change. *Climatic Change*, *131*(1), 51–66. https://doi.org/10.1007/s10584-014-1112-5

Monier, E., Sokolov, A. P., Schlosser, C. A., Scott, J. R., & Gao, X. (2013). Probabilistic projections of 21st century climate change over northern Eurasia. *Environmental Research Letters*, *8*(4), 045008. https://doi.org/10.1088/1748-9326/8/4/045008

Morice, C. P., Kennedy, J. J., Rayner, N. A., & Jones, P. D. (2012). Quantifying uncertainties in global and regional temperature change using an ensemble of observational estimates: The HadCRUT4 dataset. *Journal of Geophysical Research*, *117*, D08101. https://doi.org/10.1029/2011JD017187

Norby, R. J., DeLucia, E. H., Gielen, B., Calfapietra, C., Giardina, C. P., King, J. S., et al. (2005). Forest response to elevated CO_2 is conserved across a broad range of productivity. *PNAS*, *102*(50), 18,052–18,056. https://doi.org/10.1073/pnas.0509478102

Norby, R. J., Wullschleger, S. D., Gunderson, C. A., Johnson, D. W., & Ceulemans, R. (1999). Tree responses to rising CO_2: Implications for the future forest. *Plant, Cell and Environment*, *22*(6), 683–714. https://doi.org/10.1046/j.1365-3040.1999.00391.x

Oleson, K. W., Lawrence, D. M., Bonan¸ G. B., Flanner, M.G., Kluzek¸ E., Lawrence, P.J., et al., (2010): Technical Description of version 4.0 of the Community Land Model (CLM). (NCAR Technical Note NCAR/TN-478+STR, 257 pp.). Boulder, CO: National Center for Atmospheric Research.

Olsen, S., Brasseur, G., Wuebbles, D., Barrett, S., Dang, H., Eastham, S., et al. (2013). Comparison of model estimates of the effects of aviation emissions on atmospheric ozone and methane. *Geophysical Research Letters*, *40*, 6004–6009. https://doi.org/10.1002/2013GL057660

Paltsev, S., Reilly, J. M., Jacoby, H. D., Eckaus, R. S., McFarland, J., Sarofim, M., et al. (2005). The MIT Emissions Prediction And Policy Analysis (EPPA) model: Version 4, MIT Joint Program for the Science and Policy of Global Change (Report 125, 72 pp.). Retrieved from http://web.mit.edu/globalchange/www/MITJPSPGC_Rpt125.pdf)

Pan, Y., Melillo, J. M., McGuire, A. D., Kicklighter, D. W., Pitelka, L. F., Hibbard, K., et al. (1998). Modeled responses of terrestrial ecosystems to elevated atmospheric CO_2: A comparison of simulations by the biogeochemistry models of the vegetation/ecosystem modeling and analysis project (VEMAP). *Oecologia*, *114*(3), 389–404. https://doi.org/10.1007/s004420050462

Peixoto, J. P., & Oort, A. H. (1992). *Phisics of climate* (520 pp.). New York: AIP.

Petoukhov, V., Claussen, M., Berger, A., Crucifix, M., Eby, M., Eliseev, A. V., et al. (2005). EMIC intercomparison project (EMIPCO2): Comparative analysis of EMIC simulations of climate, and of equilibrium and transient responses to atmospheric CO_2 doubling. *Climate Dynamics*. https://doi.org/10.1007/s00382-00005-00042-00383

Plattner, G., Knutti, R., Joos, F., Bickert, T., Stocker, T. F., von Bloh, W., et al. (2008). Long-term climate commitments projected with climate-carbon cycle models. *Journal of Climate*, *21*, 2721–2751.

Prinn, R., Jacoby, H., Sokolov, A., Wang, C., Xiao, X., Yang, Z., et al. (1999). Integrated global system model for climate policy assessment: Feedbacks and sensitivity studies. *Climatic Change*, *41*, 469–546.

Prinn, R., Reilly, J., Sarofim, M., Wang, C., & Felzer, B. (2007). Effects of air pollution control on climate: Results from an integrated assessment model. In M. E. Schlesinger, et al. (Eds.), *Human-induced Climate Change: An Interdisciplinary Assessment* (pp. 93–102). Cambridge, UK: Cambridge University Press.

Pu, B., & Dickinson, R. E. (2012). Examining vegetation feedbacks on global warming in the community earth system model. *Journal of Geophysical Research*, *117*, D20110. https://doi.org/10.1029/2012JD017623

Raich, J. W., Rastetter, E. B., Melillo, J. M., Kicklighter, D. W., Steudler, P. A., Peterson, B. J., et al. (1991). Potential net primary productivity in South America: Application of a global model. *Ecological Applications*, *1*(4), 399–429. https://doi.org/10.2307/1941899

Randerson, J. T., Hoffman, F. M., Thornton, P. E., Mahowald, N. M., Lindsay, K., Lee, Y.-H., et al. (2009). Systematic assessment of terrestrial biogeochemistry in coupled climate-carbon models. *Global Change Biology*, *15*, 2462–2484.

Raper, S. C. B., Gregory, J. M., & Osborn, T. J. (2001). Use of an upwelling-diffusion energy balance climate model to simulate and diagnose a/OGCM results. *Climate Dynamics*, *17*(8), 601–613. https://doi.org/10.1007/PL00007931

Reilly, J., Melillo, J., Cai, Y., Kicklighter, D., Gurgel, A., Paltsev, S., et al. (2012). Using land to mitigate climate change: Hitting the target, recognizing the tradeoffs. *Environmental Science and Technology*, *46*(11), 5672–5679. https://doi.org/10.1021/es2034729

Reilly, J., Paltsev, S., Felzer, B., Wang, X., Kicklighter, D., Melillo, J., et al. (2007). Global economic effects of changes in crops, pasture and forests due to changing climate, carbon dioxide and ozone. *Energy Policy*, *35*(11), 5370–5383. https://doi.org/10.1016/j.enpol.2006.01.040

Richardson, M., Cowtan, K., Hawkins, E., & Stolpe, M. B. (2016). Reconciled climate response estimates from climate models and the energy budget of Earth. *Nature Climate Change*, *6*(10), 931–935. https://doi.org/10.1038/nclimate3066

Rogelj, J., Meinshausen, M., & Knutti, R. (2012). Global warming under old and new scenarios using IPCC climate sensitivity range estimates. *Nature Climate Change*, *2*, 248–253. https://doi.org/10.1038/nclimate1385

Russell, G. L., Miller, J. R., & Tsang, L.-C. (1985). Seasonal ocean heat transport computed from an atmospheric model. *Dynamics of Atmospheres and Oceans*, *9*(3), 253–271. https://doi.org/10.1016/0377-0265(85)90022-3

Saikawa, E., Schlosser, C. A., & Prinn, R. G. (2013). Global modeling of soil N_2O emissions from natural processes. *Global Biogeochemical Cycles*, *27*, 972–989. https://doi.org/10.1002/gbc.20087

Sato, M., Hansen, J. E., McCormick, M. P., & Pollack, J. B. (1993). Stratospheric aerosol optical depths. *Journal of Geophysical Research*, *98*, 22, 987–22 944. https://doi.org/10.1029/93JD02553

Schlosser, C. A., Gao, X., Strzepek, K., Sokolov, A., Forest, C. E., Awadalla, S., & Farmer, W. (2013). Quantifying the likelihood of regional climate change: A hybridized approach. *Journal of Climate*, *26*(10), 3394–3414. https://doi.org/10.1175/JCLI-D-11-00730.1

Schlosser, C. A., Kicklighter, D., & Sokolov, A. (2007). A global land system framework for integrated climate-change assessments. MIT Joint Program for the Science and Policy of Global Change (Report 147, 82 pp.). Retrieved from http://web.mit.edu/globalchange/www/MITJPSPGC_Rpt147.pdf

Schlosser, C. A., Strzepek, K., Gueneau, A., Fant, C., Gao, X., Blanc, E., et al. (2014). The future of global water stress: An integrated assessment. *Earth's Future*, *2*(8), 341–361. https://doi.org/10.1002/2014EF000238

Smith, S. J., van Aardenne, J., Klimont, Z., Andres, R. J., Volke, A., & Arias, S. D. (2011). Anthropogenic sulfur dioxide emissions: 1850–2005. *Atmospheric Chemistry and Physics*, *11*, 1101–1116.

Smith, T. M., Arkin, P. A., Ren, L., & Shen, S. S. (2012). Improved reconstruction of global precipitation since 1900. *Journal of Atmospheric and Oceanic Technology*, *29*(10), 1505–1517. https://doi.org/10.1175/JTECH-D-12-00001.1

Sokolov, A., Forest, C. E., & Stone, P. H. (2003). Comparing oceanic heat uptake in AOGCM transient climate change experiments. *Journal of Climate*, *16*(10), 1573–1582. https://doi.org/10.1175/1520-0442-16.10.1573

Sokolov, A., & Stone, P. H. (1998). A flexible climate model for use in integrated assessments. *Climate Dynamics*, *14*(4), 291–303. https://doi.org/10.1007/s003820050224

Sokolov, A., Stone, P. H., Forest, C. E., Prinn, R. G., Sarofim, M. C., Webster, M., et al. (2009). Probabilistic forecast for 21st century climate based on uncertainties in emissions (without policy) and climate parameters. *Journal of Climate*, *22*(19), 5175–5204. https://doi.org/10.1175/2009JCLI2863.1

Sokolov, A. P. (2006). Does model sensitivity to changes in CO_2 provide a measure of sensitivity to other forcings? *Journal of Climate*, *19*(13), 3294–3306. https://doi.org/10.1175/JCLI3791.1

Sokolov, A. P., Dutkiewicz, S., Stone, P. H., & Scott, J. R. (2007). Evaluating the use of ocean models of different complexity in climate change studies. MIT Joint Program for the Science and Policy of Global Change (Report 128,23 pp.). Retrieved from http://web.mit.edu/globalchange/www/MITJPSPGC_Rpt128.pdf

Sokolov, A. P., Kicklighter, D. W., Melillo, J. M., Felzer, B. S., Schlosser, C. A., & Cronin, T. W. (2008). Consequences of considering carbon-nitrogen interactions on the feedbacks between climate and the terrestrial carbon cycle. *Journal of Climate*, *21*, 3776–3796. https://doi.org/10.1175/2008JCLI2038.1

Sokolov, A. P., & Monier, E. (2012). Changing the climate sensitivity of an atmospheric general circulation model trough cloud radiative adjustment. *Journal of Climate*, *25*(19), 6567–6584. https://doi.org/10.1175/JCLI-D-11-00590.1

Sokolov, A. P., Schlosser, C. A., Dutkiewicz, S., Paltsev, S., Kicklighter, D. W., Jacoby, H. D., et al. (2005). The MIT Integrated Global System Model (IGSM) Version 2: Model description and baseline evaluation, MIT Joint Program for the Science and Policy of Global Change Report 124 (40 pp.). Retrieved from http://web.mit.edu/globalchange/www/MITJPSPGC_Rpt124.pdf

Sokolov, A. P., & Stone, P. H. (1995). Description and validation of the MIT version of the GISS 2-D model. MIT Joint Program for the Science and Policy of Global Change (Report 2, 23 pp.). Retrieved from https://globalchange.mit.edu/publication/13844

Stocker, T. F., Broecker, W. S., & Wright, D. G. (1994). Carbon uptake experiments with a zonally-averaged global ocean circulation model. *Tellus*, *46B*, 103–122.

Stone, P. H., & Yao, M.-S. (1987). Development of a two-dimensional zonally averaged statistical-dynamical model. II: The role of eddy momentum fluxes in the general circulation and their parameterization. *Journal of the Atmospheric Sciences*, *44*(24), 3769–3786. https://doi.org/10.1175/1520-0469(1987)044<3769:DOATDZ>2.0.CO;2

Stone, P. H., & Yao, M.-S. (1990). Development of a two-dimensional zonally averaged statistical-dynamical model. III: The parameterization of the eddy fluxes of heat and moisture. *Journal of Climate*, *3*(7), 726–740. https://doi.org/10.1175/1520-0442(1990)003<0726:DOATDZ>2.0.CO;2

Stouffer, R. J., Yin, J., Gregory, J. M., Dixon, K. W., Spelman, M. J., Hurlin, W., et al. (2006). Investigating the causes of the response of the thermohaline circulation to past and future climate changes. *Journal of Climate*, *19*(8), 1365–1387. https://doi.org/10.1175/JCLI3689.1

Swenson, S. C., Lawrence, D. M., & Lee, H. (2012). Improved simulation of the terrestrial hydrological cycle in permafrost regions by the community land model. *Journal of Advances in Modeling Earth Systems*, *4*, M08002. https://doi.org/10.1029/2012MS000165

Tatang, M. A., Pan, W., Prinn, R. G., & McRae, G. J. (1997). An efficient method for parametric uncertainty analysis of numerical geophysical models. *Journal of Geophysical Research*, *102*, 21,925–21,932. https://doi.org/10.1029/97JD01654

Taylor, K. E., Stouffer, R. J., & Meehl, G. A. (2012). An overview of CMIP5 and the experiment design. *Bulletin of the American Meteorological Society*, *93*(4), 485–498. https://doi.org/10.1175/BAMS-D-11-00094.1

Tian, H., Melillo, J. M., Kicklighter, D. W., McGuire, A. D., & Helfrich, J. (1999). The sensitivity of terrestrial carbon storage to historical climate variability and atmospheric CO_2 in the United States. *Tellus, B*, *51*(2), 414–452. https://doi.org/10.1034/j.1600-0889.1999.00021.x

Tseng, Y. H., Chien, S.-H., Jin, J., & Miller, N. L. (2012). Modeling air-land-sea interactions using the integrated regional model system in Monterey Bay, California. *Monthly Weather Review*, *140*(4), 1285–1306. https://doi.org/10.1175/MWR-D-10-05071.1

Vano, J. A., Das, T., & Lettenmaier, D. P. (2012). Hydrologic sensitivities of Colorado River runoff to changes in precipitation and temperature. *Journal of Hydrometeorology*, *13*(3), 932–949. https://doi.org/10.1175/JHM-D-11-069.1

Wang, C. (2004). A modeling study on the climate impacts of black carbon aerosols. *Journal of Geophysical Research*, *109*, D03106. https://doi.org/10.1029/2003JD004084

Wang, C., Prinn, R. G., & Sokolov, A. (1998). A global interactive chemistry and climate model: Formulation and testing. *Journal of Geophysical Research*, *103*, 3399–3417. https://doi.org/10.1029/97JD03465

Webb, M. J., Senior, C. A., Sexton, D. M. H., Ingram, W. J., Williams, K. D., Ringer, M. A., et al. (2006). On the contribution of local feedback mechanisms to the range of climate sensitivity in two GCM ensembles. *Climate Dynamics*, *27*(1), 17–38. https://doi.org/10.1007/s00382-006-0111-2

Webster, M., Forest, C., Reilly, J., Babiker, M., Kicklighter, D., Mayer, M., et al. (2003). Uncertainty analysis of climate change and policy response. *Climatic Change*, *62*, 295–320.

Webster, M., Sokolov, A., Reilly, J., Forest, C., Paltsev, S., Schlosser, A., et al. (2012). Analysis of climate policy targets under uncertainty. *Climatic Change*, *112*(3-4), 569–583. https://doi.org/10.1007/s10584-011-0260-0

Webster, M. D., Babiker, M., Mayer, M., Reilly, J. M., Harnisch, J., Hyman, R., et al. (2002). Uncertainty in emissions projections for climate models. *Atmospheric Environment*, *36*(22), 3659–3670. https://doi.org/10.1016/S1352-2310(02)00245-5

Webster, M. D., Paltsev, S., Parsons, J., Reilly, J., & Jacoby, H. (2008). Uncertainty in greenhouse emissions and costs of atmospheric stabilization, MIT JPSPGC (Report 165). Retrieved from https://globalchange.mit.edu/sites/default/files/MITJPSPGC_Rpt165.pdf

Williams, K. D., Ringer, M. A., Senior, C. A., Webb, M. J., McAvaney, B. J., Andronova, N., et al. (2006). Evaluation of a component of the cloud response to climate change in an intercomparison of climate models. *Climate Dynamics*, *26*(2–3), 145–165. https://doi.org/10.1007/s00382-005-0067-7

Xiao, X., Kicklighter, D. W., Melillo, J. M., McGuire, A. D., Stone, P. H., & Sokolov, A. P. (1997). Linking a global terrestrial biogeochemical model and a 2-dimensional climate model: Implications for the global carbon budget. *Tellus B*, *49*(1), 18–37. https://doi.org/10.3402/tellusb.v49i1.15948

Xiao, X., Melillo, J. M., Kicklighter, D. W., McGuire, A. D., Prinn, R. G., Wang, C., et al. (1998). Transient climate change and net ecosystem production of the terrestrial biosphere. *Global Biogeochemical Cycles*, *12*, 345–360. https://doi.org/10.1029/98GB01035

Xin, Y. F., Wu, B. Y., Bian, L. G., Liu, G., Zhang, L., & Li, R. (2012). Response of the east Asian climate system to water and heat changes of global frozen soil using NCAR CAM model. *Chinese Science Bulletin*, *57*(34), 4462–4471. https://doi.org/10.1007/s11434-012-5361-2

Zampieri, M., Serpetzoglou, E., Anagnostou, E. N., Nikolopoulos, E. I., & Papadopoulos, A. (2012). Improving the representation of river-groundwater interactions in land surface modeling at the regional scale: Observational evidence and parameterization applied in the community land model. *Journal of Hydrology*, *420*, 72–86.

Zhang, S. L., Shi, J., & Dou, Y. (2012). A soil moisture assimilation scheme based on the microwave land emissivity model and the community land model. *International Journal of Remote Sensing*, *33*(9), 2770–2797. https://doi.org/10.1080/01431161.2011.620032

Zhu, Q., & Zhuang, Q. (2013). Modeling the effects of organic nitrogen uptake by plants on the carbon cycling of boreal forest and tundra ecosystems. *Biogeosciences*, *10*(12), 7943–7955. https://doi.org/10.5194/bg-10-7943-2013

Zhu, X., Zhuang, Q., Chen, M., Sirin, A., Melillo, J., Kicklighter, D., et al. (2011). Rising methane emissions in response to climate change in northern Eurasia during the 21st century. *Environmental Research Letters*, *6*(4), 1–9. https://doi.org/10.1088/1748-9326/6/4/045211

Zhu, X., Zhuang, Q., Qin, Z., Glagolev, M., & Song, L. (2013). Estimating wetland methane emissions from the northern high latitudes from 1990 to 2009 using artificial neural networks. *Global Biogeochemical Cycles*, *27*, 592–604. https://doi.org/10.1002/gbc.20052

Zhuang, Q., Melillo, J. M., Kicklighter, D. W., Prinn, R. G., McGuire, A. D., Steudler, P. A., et al. (2004). Methane fluxes between terrestrial ecosystems and the atmosphere at northern high latitudes during the past century: A retrospective analysis with a process-based biogeochemistry model. *Global Biogeochemical Cycles*, *18*, GB3010. https://doi.org/10.1029/2004GB002239

Zickfeld, K., Eby, M., Weaver, A. J., Alexander, K., Crespin, E., Edwards, N. R., et al. (2013). Long-term climate change commitment and reversibility: An EMIC intercomparison. *Journal of Climate*, *26*(16), 5782–5809. https://doi.org/10.1175/JCLI-D-12-00584.1

Erratum

In the originally published version of this article, there was an error in the title, "Description and Evaluation of the MESM" should have been published as "Description and Evaluation of the MIT Earth System Model (MESM)". The error has since been corrected and this version may be considered the authoritative version of record.